iScience

CellPress
OPEN ACCESS

Article

Hydrogenative coupling of nitriles with diamines to benzimidazoles using lignin-derived Rh_2P catalyst

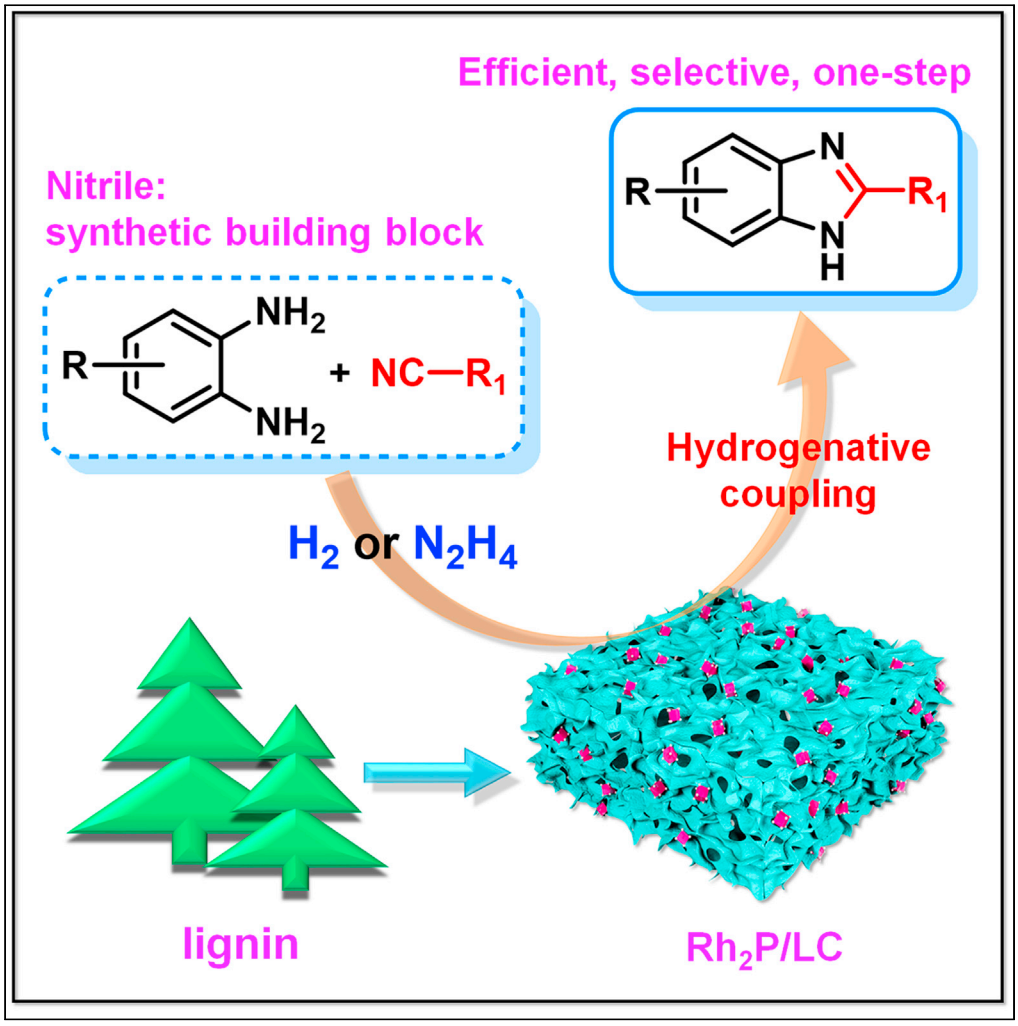

Jiarui Zhang, Ruxu Yao, Jinzhu Chen, Tao Li, Yisheng Xu

chenjz@jnu.edu.cn (J.C.)
tli@ecust.edu.cn (T.L.)
yshxu@ecust.edu.cn (Y.X.)

Highlights

Nitrile was developed as synthetic building block for organic synthesis

Reductive coupling of nitriles to 1,2-phenylenediamines yielded benzimidazoles

Strong P—Rh interaction and charge transfer to Rh enhanced Rh_2P activity

H/D exchange between H_2 and $-CD_3$ in CD_3CN occurred via intramolecular D-shift

Zhang et al., iScience 24, 103045
September 24, 2021
https://doi.org/10.1016/j.isci.2021.103045

iScience

CellPress
OPEN ACCESS

Article

Hydrogenative coupling of nitriles with diamines to benzimidazoles using lignin-derived Rh_2P catalyst

Jiarui Zhang,[1,2,3] Ruxu Yao,[1,2,3] Jinzhu Chen,[2,4,*] Tao Li,[1,*] and Yisheng Xu[1,*]

SUMMARY

Nitrile (C≡N bond) activation for direct organic synthesis has been less explored so far due to a high redox potential of nitrile and its low dissociation energy of C−CN bond. Herein, we demonstrate a direct reductive coupling of nitriles and 1,2-phenylenediamines to yield various benzimidazoles in excellent yields (95%–99%) by using rhodium phosphide (Rh_2P) catalyst supported on lignin-derived carbon (LC) using H_2 (or hydrazine hydrate) as a hydrogen source. The high catalytic performance of Rh_2P/LC is attributed to enhanced charge transfer to Rh and strong P−Rh interactions. Our isotope trace experiment confirms the presence of H/D exchange between H_2 and the inert $-CD_3$ group of CD_3CN *via* an intramolecular D-shift. Reusability of Rh_2P/LC is further demonstrated by a seven-time recycling without evident loss of activity. This research thus highlights a great potential in organic transformation with nitrile as a synthetic building block.

INTRODUCTION

Benzimidazole and its derivatives are pharmaceutically important heterocyclic compounds with a broad range of biological activities and pharmacological properties such as anti-viral, anti-fungal, anti-bacterial, anti-ulcer, anti-inflammatory, anti-hypertensive, anti-histaminic, anti-cancer, anti-tumor, and anti-HIV features (Chakrabarti et al., 2019; Keri et al., 2015). Their synthetic methods have received extensive attention due to their pharmaceutical importance. Benzimidazoles are traditionally prepared according to Ladenburg ring closure method (Scheme 1A) by direct condensation of 1,2-phenylenediamines (**1**) with carboxylic acids and their derivatives such as acids, acyl chlorides, anhydrides, aldehydes, amides and nitriles in the presence of strong acid at high reaction temperature. Among these carboxylic acid derivatives, due to a facile access to nitriles and their high availability as commodity chemicals, direct condensation of **1** with nitriles should have great potential in synthetic chemistry of benzimidazoles and in the productions of benzimidazole-related agrochemicals and pharmaceuticals (Dalziel et al., 2018; Le Questel et al., 2000; Tamura et al., 2013).

Unfortunately, research on direct condensation of **1** and nitriles is very limited. According to the reported results (Hölljes and Wagner, 1944), 27% yield of 2-methylbenzimidazole (**3a**) was obtained from 1,2-phenylenediamine (**1a**) and acetonitrile (**2a**) in the presence of an equivalent of anhydrous hydrogen chloride (HCl) in a sealed tube at 200°C for six hours (Scheme 1C). The corresponding condensation reaction mechanism suggests an initial formation of highly reactive ammonoacyl chloride (**4**, Scheme 2A) from nitrile (**2**) and HCl under anhydrous conditions. The *in situ* formed **4** smoothly promotes subsequent ring closure to yield benzimidazoles (**3**). Therefore, nitrile activation, *via* additively uniting with HCl (**4**, Scheme 2A) at 200°C, is a prerequisite for the condensation reaction. However, nitrile (C≡N bond) activation has been less explored so far when compared with C=C, C=O, C=N and O−N=O bonds owing to the high redox potential of nitriles and the low dissociation energy of C−CN bond.

Most recently, nitrile hydrogenation was developed for atom-economic synthesis of amine with transition-metal-based catalysts (Bagal and Bhanage, 2015; Werkmeister et al., 2014; Liu et al., 2018a; Nandi et al., 2017) (Table S1). However, a crucial selectivity issue arises from an inevitable formation of mixtures of primary (**7**), secondary (**9**) and tertiary amines (**10**) with alkylimines (**6**) and dialkylimines (**8**) as the proposed reactive intermediates (Scheme 2B). High reactivity of these reaction intermediates (**6** and **8**) competitively

[1]State Key Laboratory of Chemical Engineering, International Joint Research Center of Green Energy Chemical Engineering, East China University of Science and Technology, Shanghai 200237, China

[2]College of Chemistry and Materials Science, Guangdong Provincial Key Laboratory of Functional Supramolecular Coordination Materials and Applications, Jinan University, Guangzhou 511443, China

[3]These authors contributed equally

[4]Lead contact

*Correspondence: chenjz@jnu.edu.cn (J.C.), tli@ecust.edu.cn (T.L.), yshxu@ecust.edu.cn (Y.X.)

https://doi.org/10.1016/j.isci.2021.103045

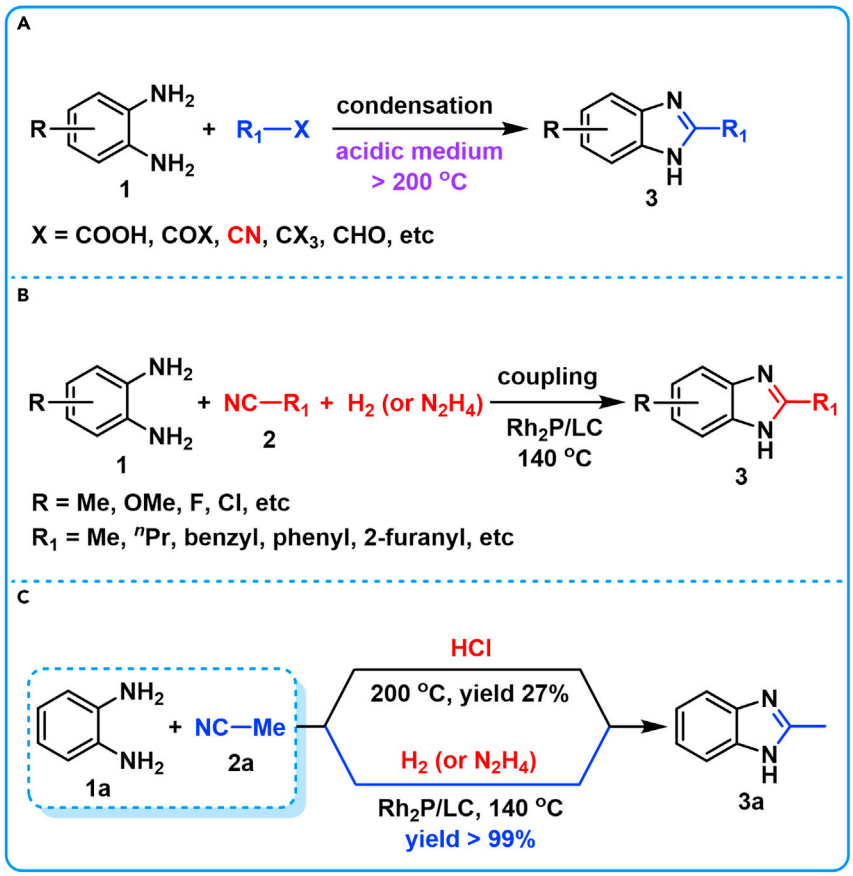

Scheme 1. Methods for benzimidazole syntheses

(A) Traditional condensation.

(B) Present reductive coupling.

(C) Comparison of condensation and coupling method.

induces a series of parallel and consecutive reactions, resulting in a challenge of selectivity control and product separation. Generally, nitrile hydrogenation can be performed under relatively mild reaction conditions (20–140°C). We thus think that the presence of **1** in the nitrile-hydrogenation system should be able to trap the *in situ* formed two reactive imines intermediates (**6** and **8**) to give *N*-(*o*-aminopheny)-imine intermediate (**11**, Scheme 2B). A subsequent cyclization of **11** and successive dehydrogenation of the resulting ring-closing product (**12**, Scheme 2B) should yield **3** under the reaction conditions (Scheme 2B). Therefore, a transition-metal-promoted reductive coupling of nitriles and 1,2-phenylenediamines was investigated in this research for green and atom-economic synthesis of benzimidazoles (Scheme 2B).

As shown in Scheme 2B, the reductive coupling process should be initialized from catalytic hydrogenation of nitriles. Both heterogeneous and homogeneous catalysts were reported for nitriles hydrogenation. Precious metal-complex-based homogeneous catalysts evidently show excellent catalytic performance on the hydrogenation (Bagal and Bhanage, 2015; Werkmeister et al., 2014; Chakraborty and Berke, 2014; Hou et al., 2020; Islam et al., 2010; Liu et al., 2018b; Chakraborty and Milstein, 2017). Although the developed heterogeneous catalysts are very limited and generally suffer from low activity, low selectivity, and low tolerance to functional group when compared with homogeneous catalysts (Wang et al., 2019; Huang and Sachtler, 1999a, 1999b; Zhang et al., 2019; Monguchi et al., 2017; Li et al., 2012; Carothers and Jones, 1925; Braos-García et al., 2010). Efforts to explore efficient catalytic systems with excellent recyclability have always been going on for industrial purpose.

Rhodium-phosphine complexes are highly efficient for nitrile hydrogenation among various investigated homogeneous catalysts. While, rhodium phosphide (Rh_2P) crystal shows surface Rh atoms surrounded

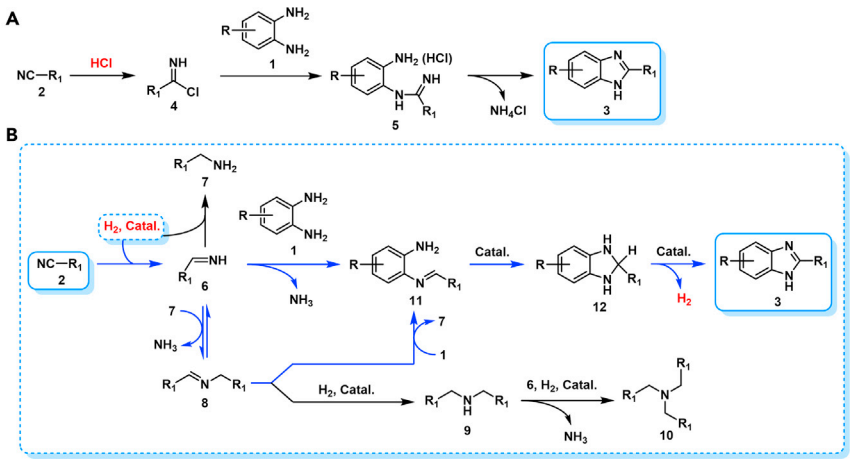

Scheme 2. Proposed reaction mechanism for 3 formation

(A) HCl-induced condensation.

(B) transition-metal-promoted reductive coupling.

by two coordinated P atoms, which is sterically and structurally similar to the Rh-P interactions in bisphosphine ligand-modified Rh complexes. Moreover, integrating P atoms into the lattices of Rh metal can tune its internal electronic structure, thus improving the intrinsic catalytic activity of the resulting Rh_2P catalyst (Shi and Zhang, 2016; Zhuang et al., 2016). Currently, Rh_2P is developed as an excellent heterogeneous catalyst for hydrogenation, hydrodeoxygenation, hydroformylation, hydrodesulfurization, and hydrodenitrogenation (Luo et al., 2020; Griffin et al., 2017; Alvarado Rupflin et al., 2017; Hayes et al., 2010).

Herein, we demonstrated the first example of a reductive coupling of nitriles and 1,2-phenylenediamines to 2-alkylbenzimidazoles (Scheme 1B) by using Rh_2P catalyst (Rh_2P/LC) supported on lignin-derived hierarchically porous carbon (LC, Figure 1). The lignin was selected as precursor of the catalyst support due to its unique structure of three-dimensional and porous framework, rich in carbon-oxygen-based functional groups on the framework, scalable and renewable nature as a carbon-based feedstock (Zhu et al., 2019; Chatterjee and Saito, 2015). The developed Rh_2P/LC demonstrates high efficiency by coupling serial tandem reactions of nitrile hydrogenation, **11** cyclization and **12** dehydration in one-pot (Scheme 2B). In contrast to traditional condensation method (Feng et al., 2016; Wade et al., 2015; Shiraishi et al., 2010; Wang et al., 1997; Selvam et al., 2009) (Table S2), Rh_2P/LC promoted reductive coupling of **1a** and **2a** can readily perform at 140°C with >99% yield of **3a** by using H_2 or hydrazine hydrate ($N_2H_4 \cdot H_2O$) as hydrogen sources (Scheme 1C).

RESULTS AND DISCUSSION

Catalyst preparation and characterization

In this research, LC was used as catalyst support, which was obtained by calcination a mixture of enzymatic hydrolysis lignin (EHL) and potassium bicarbonate ($KHCO_3$) at 800°C under atmospheric N_2, followed by thoroughly leaching with aqueous HCl solution. While, Rh_2P/LC_{400} catalyst was prepared by co-loading $RhCl_3$ and bis(diphenylphosphino)ethane (dppe) ligand on the resulting LC surface, followed by a pyrolysis at 400°C under atmospheric H_2/N_2. The subscript 400 in Rh_2P/LC_{400} indicates the final calcination temperature for catalyst preparation. The introduced dppe ligand provides P source for the formation of Rh_2P species on the LC support during calcination procedure. For comparison, Rh catalyst (Rh/LC_{400}) supported on LC was prepared without addition of the dppe ligand to investigate the electronic effect of the introduced P on the catalytic performance of the resulting Rh_2P catalyst. Moreover, to understand the influence of metallic site on the reductive coupling, Pd (Pd/LC_{400}) and Ru (Ru/LC_{400}) catalysts were synthesized with same method to Rh_2P/LC_{400}; however, the expected metal phosphides of Pd-P and Ru-P samples were undetected on the resulting catalyst surfaces.

The morphology of the obtained samples was initially characterized by scanning electron microscopy (SEM) and transmission electron microscopy (TEM). EHL shows a bulky, solid, and compact architecture

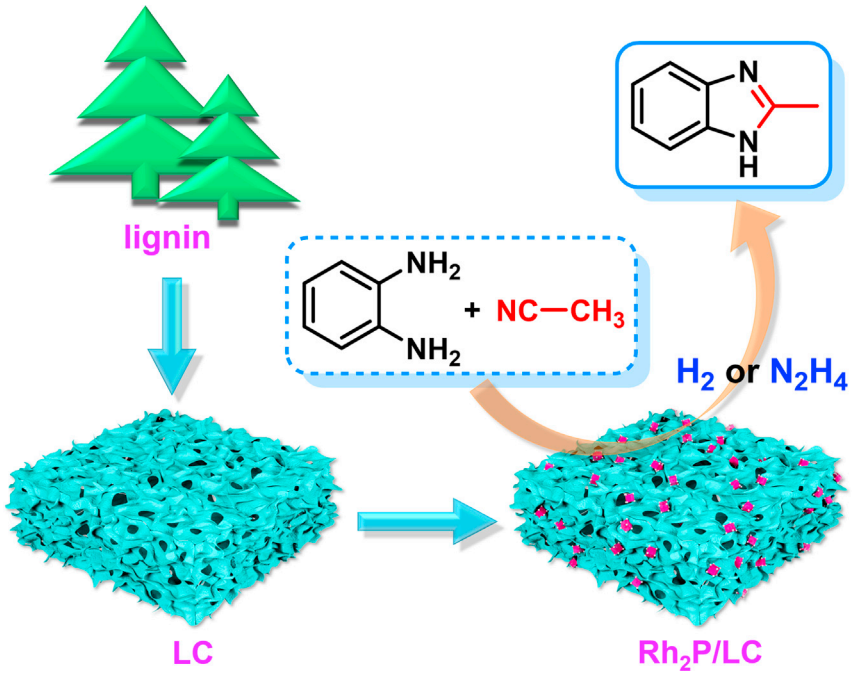

Figure 1. Rh_2P/LC-promoted reductive coupling 1a with 2a

with irregular shapes and rough surface based on the SEM analysis (Figure S1A). While, the resulting LC exhibits a sponge-like structure with readily accessible, highly crosslinked and randomly opened macropores (Figures S1B and S1C). After Rh_2P loading, the obtained Rh_2P/LC_{400} possesses similar SEM micrograph to that of LC (Figure S1D). The TEM of Rh_2P/LC_{400} exhibits ultrathin carbon nanosheet-assembled three-dimensional (3D) network with a crumpled, wrinkled, and rippled structure (Figure 2A). Additionally, Rh, P, and C elements are homogeneously and highly dispersed on the detected area of LC surface as shown by the TEM energy-dispersive X-ray (EDX) images of Rh_2P/LC_{400} (Figure 2M–2P). The estimated average nanoparticle size of Rh_2P was 4.3 nm (Figure 2B) with a detectable crystal fringe spacing of 0.280 nm, corresponding to the (200) crystal plane of Rh_2P (Su et al., 2020) (Figure 2C).

In the case of Rh/LC_{400}, its TEM images reveal a mean Rh nanoparticle size of 7.4 nm (Figures 2D and 2E) with lattice fringe spacing of 0.220 nm (Figure 2F), which can be indexed to the (111) plane of the Rh (Su et al., 2020). The TEM images of Pd/LC_{400} indicate a significantly increased average size to 18.3 nm for Pd nanoparticle on the LC support (Figures 2G and 2H). The observed lattice fringe spacing was detected as 0.224 nm, belonging to the (111) plane of Pd (Sun et al., 2020) (Figure 2I). Finally, for Ru/LC_{400} sample, TEM images show an average nanoparticle size of 3.3 nm (Figures 2J and 2K) with the lattice fringe spacing around 0.214 nm, corresponding to the (002) plane of Ru (Wang et al., 2020) (Figure 2L). Therefore, the average nanoparticle size decreased in the order of Pd > Rh > Rh_2P > Ru among the investigated samples. Moreover, Rh_2P/LC_{400} exhibits much smaller size of Rh nanoparticle with more homogeneous and more uniform dispersion if compared with Rh/LC_{400} (Figures 2A–2F). The observed porous architecture of Rh_2P/LC_{400} should be favorable for mass transfer and diffusion in the investigated hydrogenative coupling reaction.

The textural properties of the developed samples were investigated with N_2 sorption isotherm (Figure 3A), Table 1 lists the resulting results. LC support exhibits a steep rise at low P/P_0 zone ($P/P_0 < 0.1$) with a very weak hysteresis loop from middle to high P/P_0 zone (Figure 3A). Therefore, LC has a micropore-prevailing and hierarchically micro-mesoporous morphology (Deng et al., 2015) (Figure S2) showing a specific Brunauer-Emmet-Teller (BET) surface area around 1,664 $m^2\ g^{-1}$. After loading with transition metal, the resulting metallic catalyst exhibits a significantly reduced specific surface area (Table 1). For example, Rh_2P/LC_{400} exhibits a specific surface area of 724 $m^2\ g^{-1}$ (Table 1).

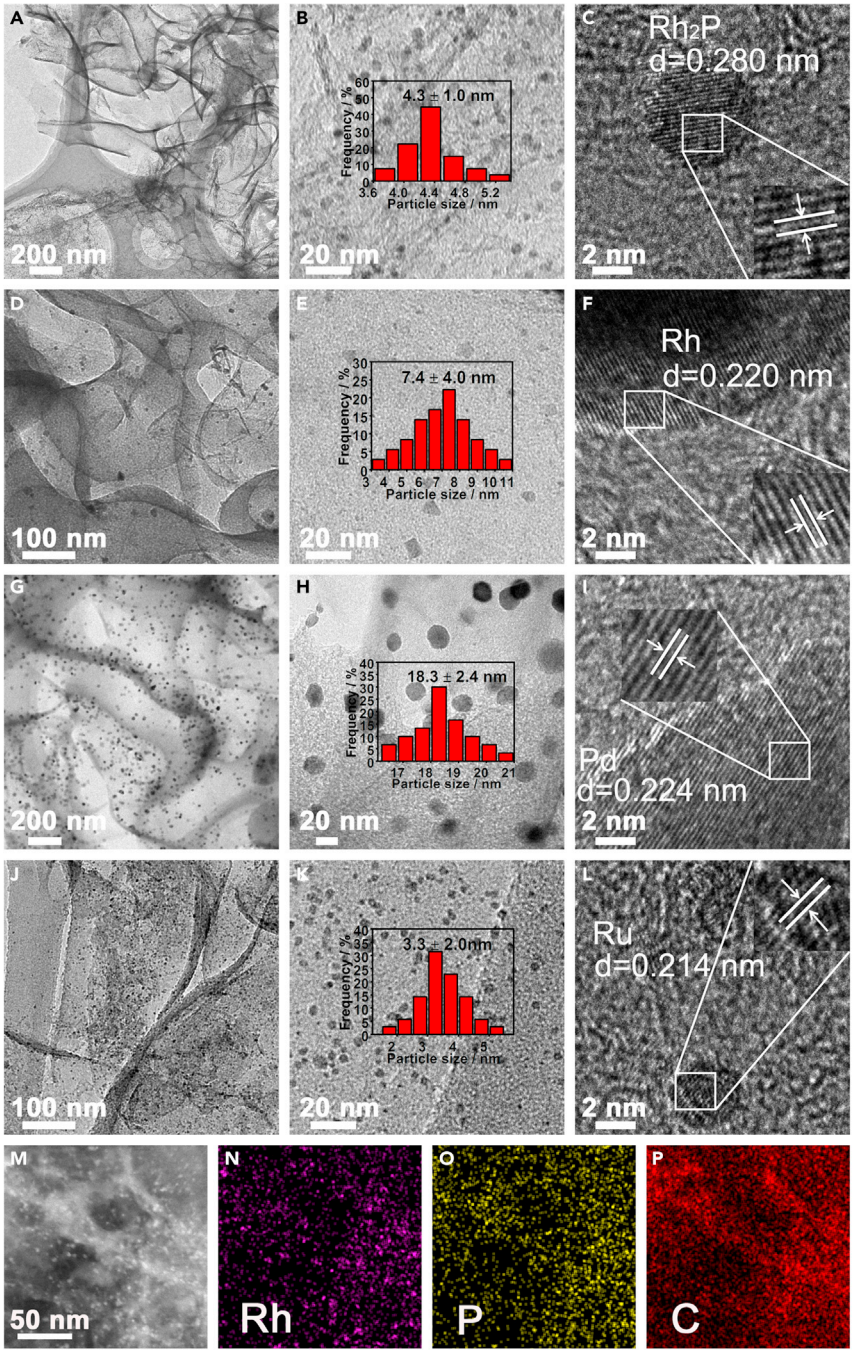

Figure 2. TEM and TEM-EDX characterizations

(A–C) TEM of Rh_2P/LC_{400}.

(D–F) TEM of Rh/LC_{400}.

(G–I) TEM of Pd/LC_{400}.

(J–L) TEM of Ru/LC_{400}.

(M–P) TEM-EDX mapping of Rh_2P/LC_{400}. Inserts of (B), (E), (H), (K) show the size distribution histogram by statistical analysis of 200 corresponding nanoparticles.

All of the obtained samples were then performed with X-ray diffraction (XRD) analysis. Rh_2P/LC_{400} shows a broad diffraction peak at 2θ = 21.0° (Figure 3B), which is indexed to the diffraction peak from amorphous carbon. In addition, five characteristic peaks at 2θ = 32.5, 46.8, 58.0, 68.2, and 77.8° are respectively

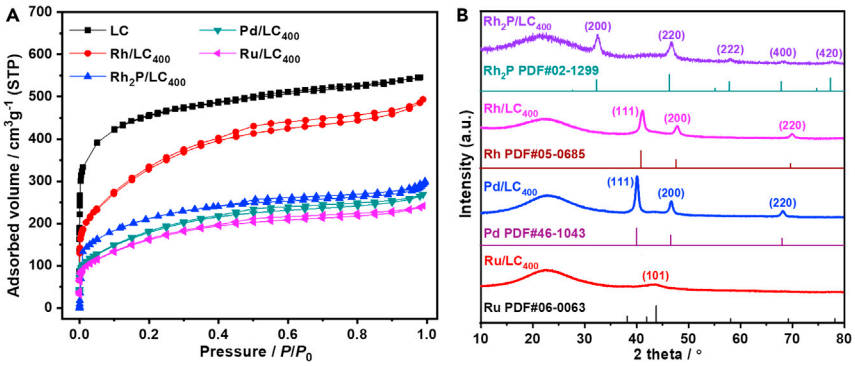

Figure 3. N_2 sorption and XRD characterizations

(A) N_2 adsorption-desorption isotherm.

(B) XRD patterns.

assigned to the (200), (220), (222), (400), and (420) planes of Rh_2P (JCPDF file no. 02-1299), suggesting the presence of Rh_2P crystal on the LC surface (Duan et al., 2017). In the case of Rh/LC_{400}, three representative diffraction peaks at 2θ values of 41.1, 47.8 and 69.9° (Figure 3B) are individually indexed to the (111), (200), and (220) planes of metallic Rh (JCPDF file no. 05-0685) (Kundu et al., 2018), which indicates successful loading of metallic Rh on the LC surface.

Pd/LC_{400} displays three characteristic peaks at 2θ = 40.2, 46.7, and 68.2° (Figure 3B), which are respectively assigned to the (111), (200), and (220) planes of metallic Pd (JCPDF file no. 46-1043). Therefore, Pd(0) crystals, rather than palladium phosphide, are suggested to be deposited on the LC surface for the obtained Pd/LC_{400} (Li et al., 2016). Notably, Ru/LC_{400} only displays a weak characteristic peak at 2θ = 44.2° (Figure 3B), corresponding to the crystalline phases of Ru (JCPDF file no. 06-0063). This observation can presumably be attributed to the highly dispersed and homogeneous Ru species with small particle size on the LC surface (Zou et al., 2019).

Surface elements and their chemical states of the obtained samples were further examined by X-ray photoelectron spectroscopy (XPS). For Rh_2P/LC_{400}, the presence of Rh, P, C, and O elements is confirmed in the XPS survey (Figure 4A and Tables S3–S7). The high-resolution Rh 3d XPS of Rh_2P/LC_{400} can be generally deconvolved into two sets of doublet peaks (Figure 4B). The set of strong doublet peaks, located at binding energies of 312.4 eV (indexed to Rh $3d_{3/2}$) and 307.7 eV (indexed to Rh $3d_{5/2}$), can be ascribed to metallic Rh, corresponding to Rh_2P species (Luo et al., 2020). The other set of weak doublet peaks at 314.8 eV (indexed to Rh $3d_{3/2}$) and 309.8 eV (indexed to Rh $3d_{5/2}$) are ascribed to the Rh(III) oxidation state (Luo et al., 2020). Rh_2P (73%) is formed as the predominant species on the Rh_2P/LC_{400} surface based on the integration areas of these two doublets, accordingly demonstrating successful formation of Rh_2P catalyst from Rh-dppe complex under the synthetic conditions. High-resolution P $2p_{3/2}$ XPS of Rh_2P/LC_{400} (Figure 4C) can be deconvoluted into three characteristic peaks at the binding energy of 134.5 eV (indexed to P−O), 133.3 eV (indexed to P−C), and 130.1 eV (indexed to Rh−P). The presence of P−O species presumably originates from oxidation of the surface P upon exposure to air, whereas the existence of P−C indicates the formation of doped P atom into the LC matrix (Chen et al., 2016). Finally, the formation of Rh_2P species can be demonstrated by the presence of Rh−P species from the P $2p_{3/2}$ XPS of Rh_2P/LC_{400}. Therefore, our XPS analysis of Rh_2P/LC_{400} is in accordance with its TEM and XRD results, confirming the major Rh_2P species on the Rh_2P/LC_{400} surface.

In the case of Rh/LC_{400}, its high-resolution Rh 3d XPS can be deconvolved into two sets of doublet peaks (Figure 4B). The set of strong doublet peaks, located at binding energies of 312.3 eV (indexed to Rh $3d_{3/2}$) and 307.6 (indexed to Rh $3d_{5/2}$), can be ascribed to metallic Rh as a prevailing species (70%), whereas the set of weak doublet peaks at 314.7 eV (indexed to Rh $3d_{3/2}$) and 309.7eV (indexed to Rh $3d_{5/2}$) are ascribed to the Rh(III) oxides. Notably, Rh_2P/LC_{400} shows evident shifts to higher binding energies in the Rh 3d XPS if compared with those of Rh/LC_{400} (Figure 4B). The observed positive shifts in the Rh 3d XPS indicate enhanced charge transfer to Rh as well as stronger interactions between P and Rh in the Rh_2P/LC_{400} sample

Table 1. Textural parameters of the investigated samples

Sample	S_{BET}[a] [$m^2\ g^{-1}$]	S_{micro}[b] [$m^2\ g^{-1}$]	S_{meso}[c] [$m^2\ g^{-1}$]	D_{micro}/D_{meso}[d] [nm]	V_{total}[e] [$cm^3\ g^{-1}$]	V_{micro}/V_{meso}[f] [$cm^3\ g^{-1}$]
LC	1664	1320	344	0.78/2.27	1.20	0.55/0.65
Rh_2P/LC_{400}	724	176	548	1.02/4.02	0.45	0.08/0.37
Rh_2P/LC_{600}	505	178	327	1.03/4.01	0.62	0.08/0.54
Rh_2P/LC_{800}	696	232	464	1.01/4.00	0.71	0.11/0.60
Rh/LC_{400}	1156	484	672	0.85/3.11	0.69	0.21/0.48
Pd/LC_{400}	630	135	495	0.85/3.08	0.41	0.12/0.29
Ru/LC_{400}	567	274	293	0.85/3.10	0.37	0.10/0.27
recovered Rh_2P/LC_{400}	426	195	231	0.60/2.05	0.33	0.10/0.23
recovered Rh/LC_{400}	797	325	472	1.01/3.99	0.57	0.16/0.41

[a] S_{BET}, specific surface area.
[b] S_{micro}, the specific surface area of micropore.
[c] Smeso, the specific surface area of mesopore.
[d] Dmicro/Dmeso, the average diameters of micropore (Dmicro) and mesopore (Dmeso).
[e] Vtotal, the total specific pore volume.
[f] Vmicro/Vmeso, the specific pore volume of micropore (Vmicro) and mesopore (Vmeso).

(Su et al., 2020). The Rh-P interaction in Rh_2P can modify the surface charge states and electron cloud density on the Rh site, which should be beneficial to H_2 activation.

For Pd/LC_{400} sample, its high-resolution Pd 3d XPS are deconvolved into two sets of doublet peaks (Figure 4D). The doublet peaks with strong intensity, located at a binding energy of 341.2 eV (indexed to Pd $3d_{3/2}$) and 336.0 eV (indexed to Pd $3d_{5/2}$), can be assigned to metallic Pd as a prevailing species (76%). The set of weak doublet peaks at 342.2 eV (indexed to Pd $3d_{3/2}$) and 337.0 eV (indexed to Pd $3d_{5/2}$) are ascribed to the Pd(II) oxides (Li et al., 2016). The high-resolution P $2p_{3/2}$ XPS of Pd/LC_{400} (Figure 4C) can be deconvoluted into two peaks, which are ascribed to P−O (134.5 eV) and P−C (133.3 eV) species.

In the case of Ru/LC_{400}, the most intensive photoemission line of Ru 3d is strongly overlapped with C 1s line from the LC support. The surface Ru species were thus examined with Ru 3p XPS. The high-resolution Ru 3p XPS were fit into two sets of doublet peaks (Figure 4E). The strong doublet peaks with binding energy of 484.0 eV (indexed to Ru $3p_{1/2}$) and 461.5 eV (indexed to Ru $3p_{3/2}$), can be assigned to metallic Ru as a predominant species (76%) (Li et al., 2020a). The set of weak doublet peaks at 486.5 eV (indexed to Ru $3p_{1/2}$) and 464.0 eV (indexed to Ru $3p_{3/2}$) are ascribed to Ru(III) oxides (Zhao et al., 2020). The high-resolution P $2p_{3/2}$ XPS peaks of Ru/LC_{400} is very close to that of Pd/LC_{400} as described above (Figure 4C).

Notably, palladium phosphide and ruthenium phosphide species were unobserved on the surfaces of Pd/LC_{400} and Ru/LC_{400}, respectively, based on TEM, XRD, and XPS analysis. Therefore, the XPS analysis further suggests that only Rh_2P/LC_{400} sample contains Rh_2P species on the LC surface although the synthetic procedure is the same for Rh_2P/LC_{400}, Pd/LC_{400} and Ru/LC_{400} samples. In the cases of Pd/LC_{400} and Ru/LC_{400} samples, the expected metal phosphide species are unobserved on the LC surface.

Hydrogenative coupling reaction

The hydrogenative coupling of 1,2-phenylenediamine (**1a**) and acetonitrile (**2a**) for 2-methyl-1*H*-benzo[*d*]imidazole (**3a**) synthesis with H_2 as hydrogen source was investigated as a model reaction to optimize reaction conditions with the obtained catalysts (Figures 5A and 5B). **3a** was unobserved under catalyst free conditions, indicating the absence of catalytic active sites for the coupling reaction. Rh/LC_{400} gave 80% yield of **3a**, which is very close to the catalytic activity of Ru/LC_{400} (83% yield, Figure 5B). A significantly increased **3a** yield to 93% was obtained by Pd/LC_{400}. However, among the investigated catalysts, Rh_2P/LC_{400} was the most efficient one by producing quantitative yield (>99%) of **3a**.

The Rh_2P/LC_{400} was obtained by pyrolysis of a mixture of $RhCl_3$, dppe and LC under H_2/N_2 at 400°C. Therefore, to probe the catalytic site of Rh_2P/LC_{400}, a mixture of $RhCl_3$−PPh_3 (PPh_3, triphenyl phosphine) and

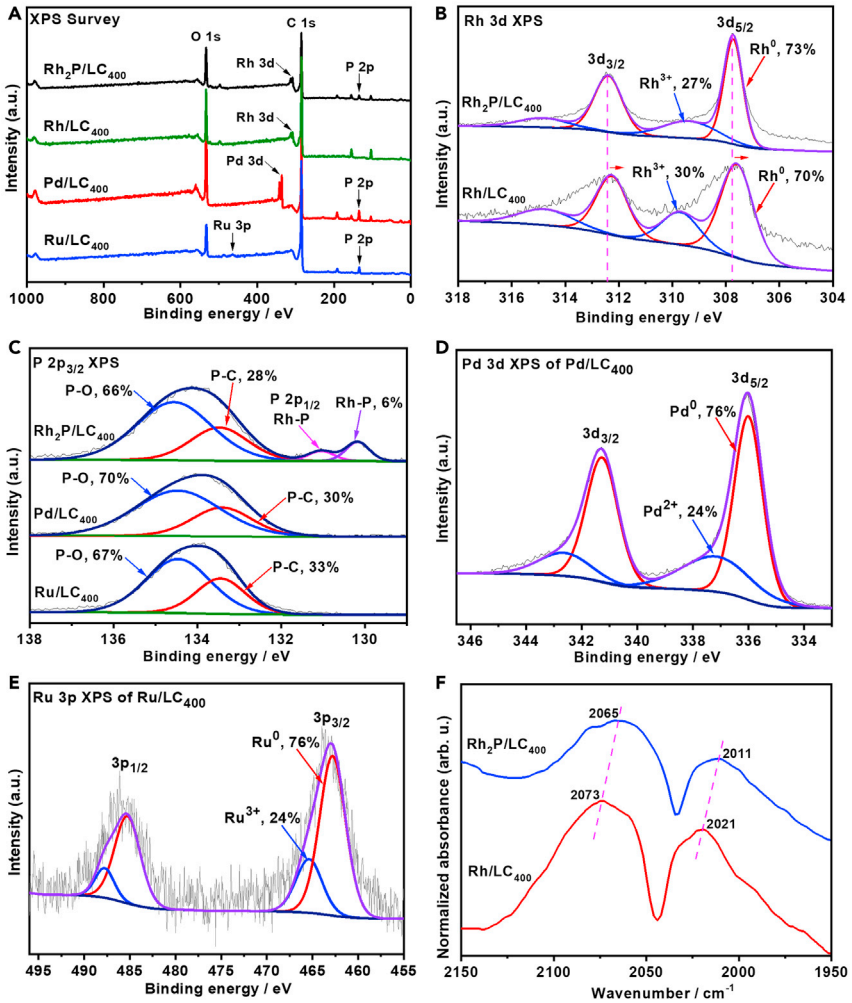

Figure 4. XPS and CO-probed FT-IR characterizations

(A) XPS scan survey of Rh_2P/LC_{400}, Rh/LC_{400}, Pd/LC_{400} and Ru/LC_{400}.

(B) Rh 3d XPS of Rh_2P/LC_{400} and Rh/LC_{400}.

(C) P $2p_{3/2}$ XPS of Rh_2P/LC_{400}, Pd/LC_{400} and Ru/LC_{400}.

(D) Pd 3d XPS of Pd/LC_{400}.

(E) Ru 3p XPS of Ru/LC_{400}.

(F) CO-probed FT-IR spectra for Rh_2P/LC_{400} and Rh/LC_{400}.

$RhCl_3$—dppe were respectively investigated as homogeneous catalysts for the coupling (Figure 5B). However, negligible **3a** yields (2–10%) were obtained with the above homogeneous system. Moreover, the reductive coupling was further carried out with Rh-based classical hydrogenation catalysts such as $Rh(PPh_3)_3Cl$ and $Rh(dppe)_2Cl$, which, again, yielded very limited amount of **3a** (5–8% yield, Figure 5B). It is thus believed that Rh_2P species, instead of Rh-P based complexes, is the true active site on the Rh_2P/LC_{400} surface for the reductive coupling reaction.

To understand the influence of pyrolysis temperature on the catalytic performance of the catalyst, the reductive coupling reaction were performed with a low loading level of Rh_2P/LC catalysts obtained at 400°C-pyrolysis (denoted as Rh_2P/LC_{400}), 600°C-pyrolysis (denoted as Rh_2P/LC_{600}), and 800°C-pyrolysis (denoted as Rh_2P/LC_{800}). Evidently, Rh_2P/LC_{400} is the most effective one for the reaction (Figure 5B). Characterization of Rh_2P/LC_{600} and Rh_2P/LC_{800} are almost the same with Rh_2P/LC_{400} (Figures S1–S3). However, a significantly increased mean nanoparticle size of Rh_2P was observed with 8.6 nm for Rh_2P/LC_{600} and 12.6 nm for Rh_2P/LC_{800}, respectively, which may presumably lead to the reduced activity. Finally, in addition to H_2,

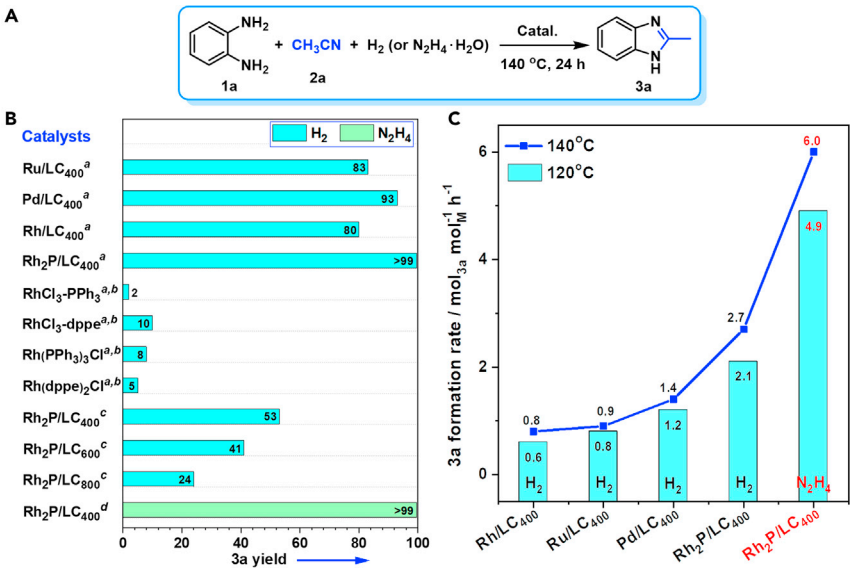

Figure 5. Catalyst screen for hydrogenative coupling

(A) Hydrogenative coupling of **1a** with CH_3CN to **3a**.

(B) Comparison of catalyst activity based on one run of each catalyst.

(C) **3a** formation rate over various catalysts. [a]Performed with catalyst (20 mg), **1a** (0.3 mmol), P_{H2} (1.0 MPa), CH_3CN (3.0 mL); [b]based on an equimolar amount of the Rh site in the Rh_2P/LC_{400} [Rh (8.0×10^{-3} mmol) and P (3.2×10^{-2} mmol)]; [c]catalyst (10 mg); [d]$N_2H_4 \cdot H_2O$ (1.0 mmol), P_{N2} (1.0 MPa), *t* (6 h).

$N_2H_4 \cdot H_2O$ was an alternative excellent hydrogen source for the reductive coupling reaction in the presence of Rh_2P/LC_{400} catalyst by producing quantitative yield of **3a** (>99%, Figure 5B).

The catalytic activities of various catalysts were further quantitatively compared based on formation rate of **3a**. In this research, **3a** formation rate in the hydrogenative coupling was obtained under a low **3a** yield around 10–15%, given as the amount of formed **3a** per amount of metal sites per hour for the investigated catalyst. Figure 5C demonstrates a comparable activity between Rh/LC_{400}, Ru/LC_{400}, and Pd/LC_{400}. Although Rh_2P/LC_{400} was proved to be the most active catalyst among various investigated samples, increase of reaction temperature slightly enhanced **3a** formation rate. Moreover, Rh_2P/LC_{400}–$N_2H_4 \cdot H_2O$ system shows a doubled activity when compared with the Rh_2P/LC_{400}–H_2 system under investigated conditions. Therefore, Rh_2P/LC_{400} exhibits superior catalytic activity over Rh/LC_{400}, presumably due to the electronic effect of Rh on the hydrogenative coupling.

2a thus functions as both reagent and solvent with an excess amount for the hydrogenative coupling under the above reaction conditions. In fact, the hydrogenative coupling can be well performed in tetrahydrofuran (THF) solvent. The influence of **2a** concentration in THF on the coupling revealed that **3a** yields increased with **2a** concentration up to 92% with an optimal **2a** concentration of 1.0 mmol mL^{-1} in THF, corresponding to 10 molar equivalents of **2a** to **1a** (Figure S4). Notably a maximal **3a** yield of 96% was obtained in THF with the **2a**/**1a** molar ratio of 30. The effect of reaction solvent on the coupling reaction demonstrated that both **2a** and THF were effective for **3a** formation (Table S8).

Electronic effect of Rh_2P

The electronic state of Rh species on Rh_2P/LC_{400} and Rh/LC_{400} was then investigated and compared by using Fourier transform infrared spectroscopy (FT-IR) with carbon monoxide (CO) as a probe molecule. The FT-IR spectra of CO-adsorbed Rh_2P/LC_{400} revealed two different CO coordination modes (Figure 4F). The band at 2065 cm^{-1} is indexed to typically terminal monocarbonyl species of Rh–CO, corresponding to the terminal CO adsorbed on metallic Rh of the Rh_2P, whereas the band at 2011 cm^{-1} is ascribed to the dicarbonyl species of $Rh(CO)_2$ (Alvarado Rupflin et al., 2017; Yates et al., 1979). In contrast, the corresponding CO coordination modes over Rh/LC_{400} are observed at 2073 cm^{-1} for Rh–CO and at 2021 cm^{-1} for $Rh(CO)_2$, respectively. Evidently, Rh_2P/LC_{400} shows blue-shifts in the CO-probed FT-IR spectra if compared

with Rh/LC_{400} (Figure 4F). The observed blue-shift indicates that Rh species on the Rh_2P/LC_{400} has weaker electron-donating capability than in the case of the Rh/LC_{400}, which suggests a decrease of electron density on the Rh site in the Rh_2P/LC_{400} due to P doping (Komanoya et al., 2017; Nakajima et al., 2013). Moreover, P doping leads to a decreased adsorption intensity of Rh_2P/LC_{400} in the CO-probed FT-IR spectra when compared with those of Rh/LC_{400}. Our Rh 3d XPS analysis for Rh_2P/LC_{400} indicates an enhanced charge transfer to Rh as well as strong interactions between P and Rh in the sample (Figure 4B). Generally, the results from CO-probed FT-IR are in line with our Rh 3d XPS analysis, suggesting a decreased electron density on Rh species in the Rh_2P/LC_{400}. Therefore, the electronic state of Rh_2P/LC_{400} may presumably affect adsorption and activation of H_2, leading to an efficient reductive coupling.

Isotope trace investigation

Hydrogenative couplings of **1a** with CH_3CN and CD_3CN were then respectively performed under H_2 with Rh_2P/LC_{400} catalyst. The proton nuclear magnetic resonance (^1H NMR) and mass spectrometry (MS) were applied to monitor the H/D exchange in the coupling process (Scheme 3A). Figure 6A shows the resulting ^1H NMR of the **3a** formed from **1a**−CH_3CN, the peak of the –NH– from **3a** was unobserved. While the signals at 7.48 ppm (*dd*, J_{HH} = 3.2, 6.0 Hz, aromatic –CH–), 7.15 ppm (*dd*, J_{HH} = 3.2, 6.0 Hz, aromatic –CH–), 2.53 ppm (*s*, $–CH_3$) were well separated in the ^1H NMR of **3a**. The resulting relative integration intensity reflected a $2_{(CH)}$:$2_{(CH)}$:$3_{(CH3)}$ ratio of proton, thus confirming the chemical structure of 2-methyl-1*H*-benzo[*d*]imidazole for the **3a**. In the case of **3a** formed from **1a**−CD_3CN, the observed aromatic –CH– signals were almost the same with those from **1a**−CH_3CN; however, the resulting signals at methyl-group region were quite complicated (Figure 6B). In addition to a singlet at 2.52 ppm ($–CH_3$), a 1:1:1 triplet (J_{HD} = 1.7 Hz) was observed at 2.50 ppm ($–CH_2D$), and a 1:2:3:2:1 quintet (J_{HD} = 1.7, 3.4 Hz) was detected at 2.49 ppm ($–CHD_2$) (Anet and O'Leary, 1989; Denny et al., 1994; Wheelhouse and Stevens, 1993; Horn and Everett, 1971). The above ^1H NMR analysis indicates the formation of mono-protonated, di-protonated and tri-protonated methyl ($–CD_nH_{3-n}$) group in **3a** with a total of 66% proton incorporation at the inert methyl carbon atoms during the **1a**−CD_3CN coupling. The molar ratio of $–CH_3$, $–CH_2D$ and $–CHD_2$ groups were 13:23:10 based on the corresponding integration areas (Figure 6B).

Figure 6C further compares the MS of **3a** formed from CH_3CN and CD_3CN. For the hydrogenative coupling of **1a**−CH_3CN, the most abundant parent molecular ions for the resulting **3a** were observed at *m/z* = 132, suggesting formation of the expected 2-methyl-1*H*-benzo[*d*]imidazole. In contrast, the **3a**, formed in **1a**−CD_3CN, contained at least three compounds of 2-methyl-1*H*-benzo[*d*]imidazole (*m/z* = 132), 2-(methyl-d_1)-1*H*-benzo[*d*]imidazole (*m/z* = 133) and 2-(methyl-d_2)-1*H*-benzo[*d*]imidazole (*m/z* = 134) with the $–CH_2D$ group-containing **3a** as the most predominant molecule. Our ^1H NMR and MS analyses thus clearly indicate the appearance of proton at the methyl group ($–CD_nH_{3-n}$) of the formed **3a** *via* the hydrogenative coupling of **1a**−CD_3CN, suggesting the presence of H/D exchange between the inert $–CD_3$ group of CD_3CN and H_2 during the CD_3CN-hydrogenation process.

Previously, propene–deuterium (C_3H_6–D_2) reaction was extensively investigated with various transition metal catalysts and equally exchangeable of all the hydrogens in C_3H_6 were observed (Hirota and Hironaka, 1965; Naito and Tanimoto, 1999). The suggested reaction mechanism involved a rate-determining step of a D_2 dissociation and subsequent incorporation of D atom into the dissociatively adsorbed intermediates such as *n*-propenyl, *sec*-propenyl and allylic species (Scheme 3B). Moreover, an intramolecular double-bond migration mechanism in propene between C1 and C3 carbon was suggested by a bridged hydrogen during the deuteration (Scheme 3C). In the case of reported CH_3CN–D_2 reaction, a series of deuterated amines such as $(CD_3CD_2)_2NH$ and $(CH_3CD_2)NH(CD_2CD_3)$ were detected by an isotope exchange of D_2 with the H atoms in $–CH_3$ group of CH_3CN (Huang and Sachtler, 1999a, 1999b). Therefore, in our case, an intramolecular D-shift may presumably promote H/D exchange between the $–CD_3$ group of CD_3CN and H_2 during the hydrogenation (Scheme 3D).

Controlled experiments and catalyst reusability

Rh_2P/LC_{400} catalyst was then selected for reductive coupling with both H_2 and $N_2H_4{\cdot}H_2O$ as hydrogen sources to probe the influence of reaction temperature and reaction time on the reaction. Reaction temperature significantly promotes the coupling reaction (Figure 7A). Negligible **3a** yields were observed below 80°C. While **3a** yields steeply increased with reaction temperature above 80°C with quantitative **3a** yield (>99%) obtained at 140°C. Regarding the influence of reaction time on the coupling (Figure 7B), $N_2H_4{\cdot}H_2O$ can remarkably reduce reaction time to 6 h by giving >99% yield of **3a**. However, a significantly

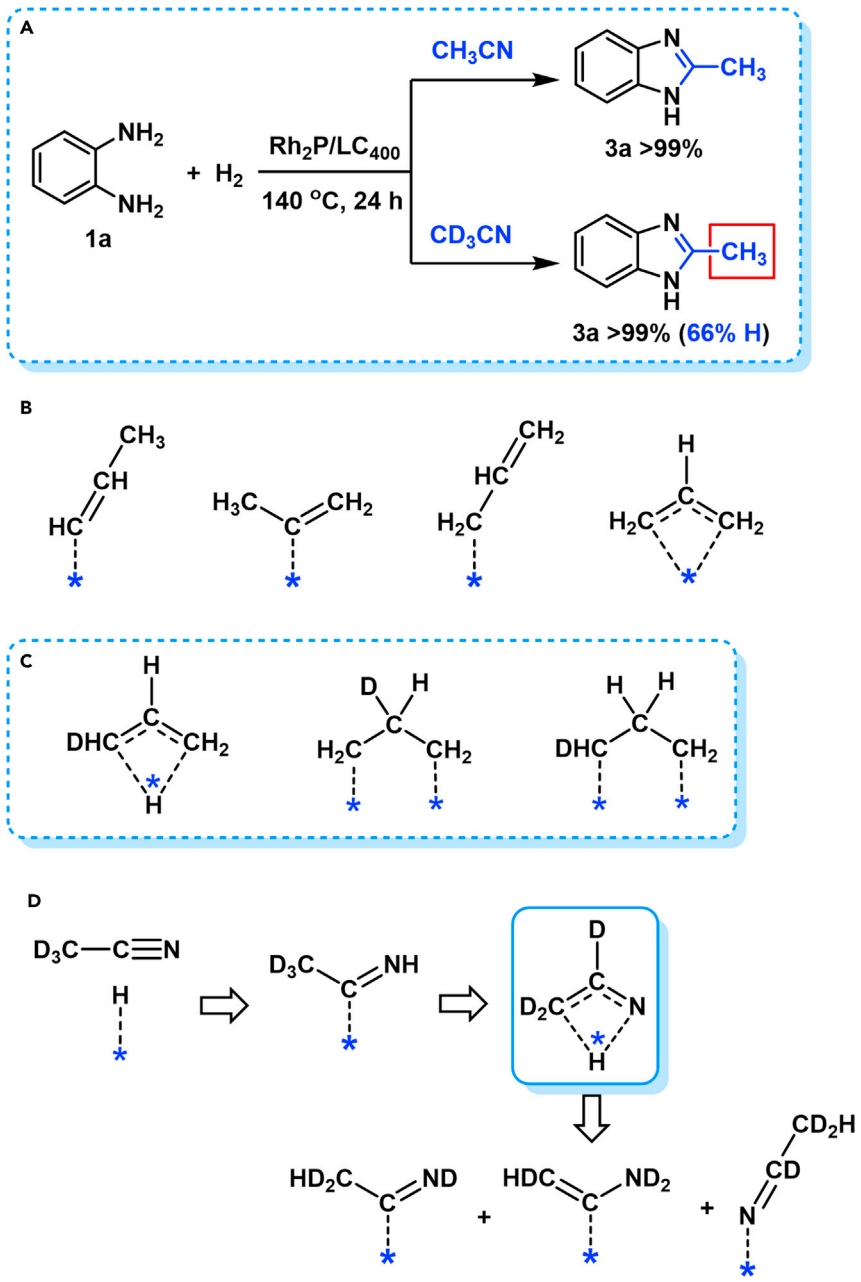

Scheme 3. Isotope trace investigation

(A) Hydrogenative coupling of 1a−CH_3CN and 1a−CD_3CN. Performed with 1a (0.3 mmol), Rh_2P/LC_{400} (20 mg), P_{H2} (1.0 MPa), CH_3CN, or CD_3CN (3.0 mL).

(B) Dissociative mechanism in C_3H_6–H_2 reaction.

(C) Intramolecular H-shift mechanism in C_3H_6–H_2 reaction.

(D) Proposed H/D exchange in CD_3CN–H_2 reaction.

prolonged reaction time to 24 h was observed for H_2 to yield quantitative **3a**. Finally, the effect of H_2 pressure on the reaction revealed that the coupling cannot occur in the absence of H_2, **3a** yield steeply increased with H_2 pressure with an optimal H_2 pressure of 1.0 MPa (Figure 7C).

The recyclability of Rh_2P/LC_{400} was subsequently examined with the hydrogenative coupling for **3a** synthesis. The recovered Rh_2P/LC_{400} was collected by vacuum filtration, thoroughly washed with ethyl alcohol,

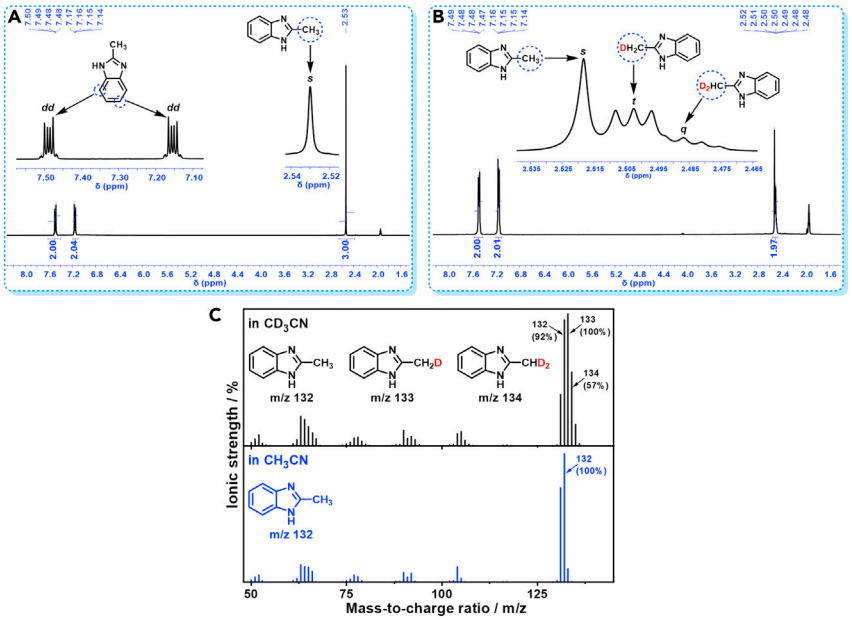

Figure 6. Comparison of 1a−CH_3CN and 1a−CD_3CN in hydrogenative coupling

(A) ^{1}H NMR spectra of **3a** from **1a**–CH_3CN.

(B) ^{1}H NMR spectra of **3a** from **1a**–CD_3CN.

(C) MS of **3a** from **1a**–CH_3CN and **1a**–CD_3CN.

dried under the vacuum, added into the autoclave, and performed with the previous reaction conditions. Noticeable decline in catalytic activity of RhP_2/LC_{400} was unobserved during the consecutive seven-time recycling (Figure 7D). Our XRD, XPS, and TEM analyses of the recovered RhP_2/LC_{400} indicated its high durability (Figure S5). However, the recovered RhP_2/LC_{400} exhibited an evidently decreased specific surface area when compared with the fresh one (Table 1 and Figure S2), presumably owing to a strong adsorption of **3a** on the RhP_2/LC_{400} surface. In addition to Rh_2P/LC_{400}, Rh/LC_{400} also showed excellent recyclability and durability during the consecutive seven-time recycling (Figures S6–S8). The above recycling experiments thus demonstrated outstanding stability of lignin-derived Rh catalysts.

Scope of the hydrogenative coupling

Therefore, we have demonstrated hydrogenative coupling of **1a**−CH_3CN for efficient synthesis of **3a** (Scheme 4). Without addition of **1a**, a direct hydrogenation of CH_3CN afforded trace amount of triethylamine (1.4% yield) with TOF of 1.1 mol_{Et3N} mol_{Rh}^{-1} h^{-1} (Scheme 4). To obtain complementary information of the hydrogenative coupling for mechanism investigation, in addition to aromatic 1,2-diamine **1a**, primary monoamines such as aniline (**13**) and benzylamine (**14**) were respectively introduced into the CH_3CN−hydrogenation system to quickly condense with the *in situ* formed ethanimine intermediate (**6**, R_1 = CH_3, Scheme 2B). In the case of **13**, both *N*-ethylaniline (**13a**) and *N,N*-diethylaniline (**13b**) were observed under the hydrogenation conditions with secondary amine (**13a**) as the major product (Scheme 4). This result is presumably attributed to weaker nucleophilicity and steric hindrance of the resulting aromatic amine **13a**, which inhibits its further reductive amination with CH_3CN. As expected, tertiary amine of *N*-benzyl-*N*-ethylethanamine (**14a**, Scheme 4) was obtained in a quantitative yield from **14** by consecutive ethylation. Finally, various aliphatic diamines such as ethylenediamine (**15**), 1,2-cyclohexanediamine (**16**), and 1,4-butanediamine (**17**) were further probed with the CH_3CN−hydrogenation system. In the cases of **15** and **16**, cyclization products of hydro-1*H*-imidazoles were unobserved, the CH_3CN−hydrogenation system directly followed ethylation pathway under the investigated conditions by yielding a mixture of stepwisely ethylated amines products (Scheme 4). For long chain aliphatic diamine **17**, similar results were observed with various ethyl-substituted amines as products. Therefore, CH_3CN functions as ethylation reagent for aromatic monoamine (**13**), aliphatic monoamine (**14**), and aliphatic diamine (**15**–**17**) *via* the reductive substitution reaction. Our research thus demonstrated that Rh_2P/LC_{400} is a versatile and efficient catalyst by hydrogenative coupling of CH_3CN with aromatic 1,2-diamine to afford benzimidazole (Scheme 4). While, hydrogenative

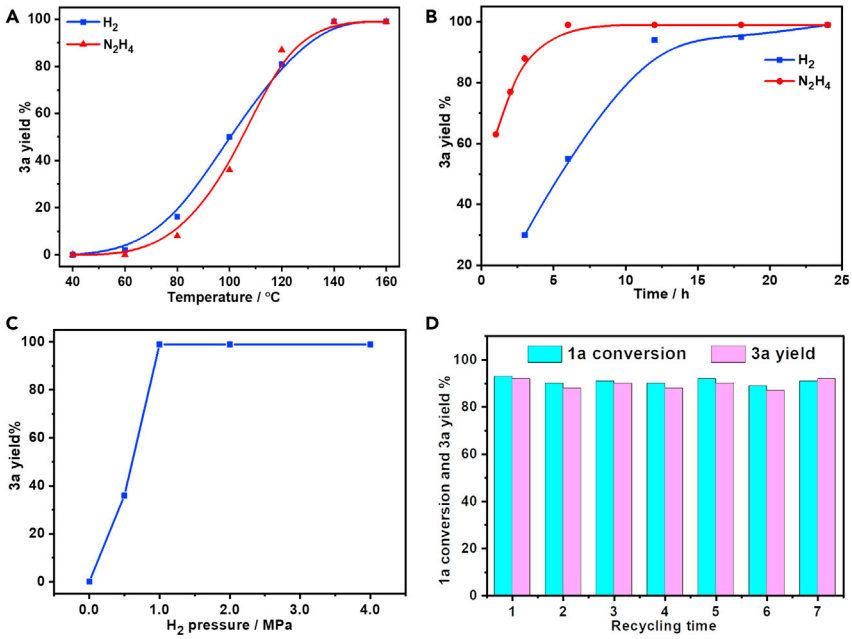

Figure 7. Reaction optimization and catalyst reusability

(A) Reaction temperature.

(B) Reaction time.

(C) Initial H_2 pressure.

(D) Reusability of Rh_2P/LC_{400}. The recovered Rh_2P/LC_{400} was collected by vacuum filtration, thoroughly washed with ethyl alcohol, dried under the vacuum, added into the autoclave, and performed with the previous reaction conditions.

Performed with: (A) Rh_2P/LC_{400} (20 mg), **1a** (0.3 mmol), CH_3CN (3.0 mL), P_{H2} (1.0 MPa) or [P_{N2} (1.0 MPa) and $N_2H_4 \cdot H_2O$ (1.0 mmol)], *t* (24 h); (B) *T* (140 °C); (C) *t* (24 h), *T* (140°C); (D) Rh_2P/LC_{400} (10 mg), **1a** (0.2 mmol).

coupling of CH_3CN with monoamine and aliphatic diamine led to formation ethyl-substituted amine. Finally, a direct hydrogenation of CH_3CN with Rh_2P/LC_{400} yielded trace amount of triethylamine.

The coupling scope was then evaluated by using Rh_2P/LC_{400} for a variety of substituted **1a** with CH_3CN under the optimal conditions (Figure 8). Various substituted **1a** were readily coupled with CH_3CN to give the

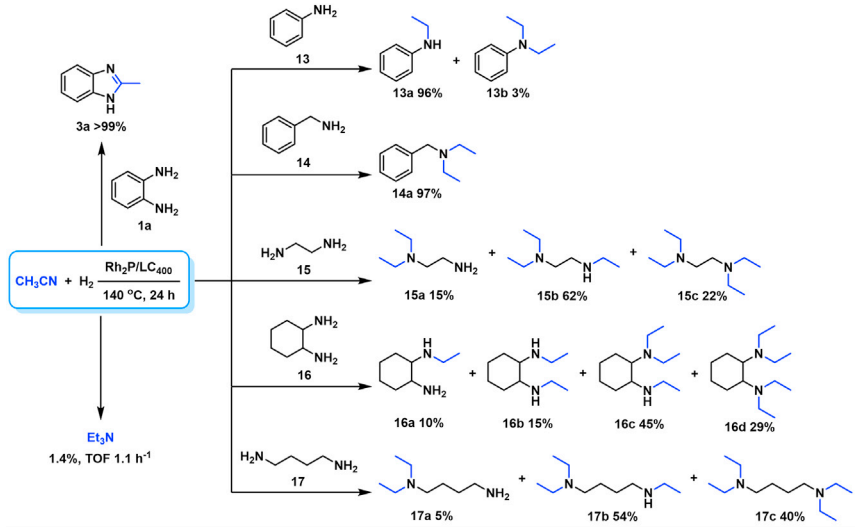

Scheme 4. Effect of amines on the hydrogenative coupling

Performed with amine (0.3 mmol), Rh_2P/LC_{400} (20 mg), P_{H2} (1.0 MPa), CH_3CN (3.0 mL).

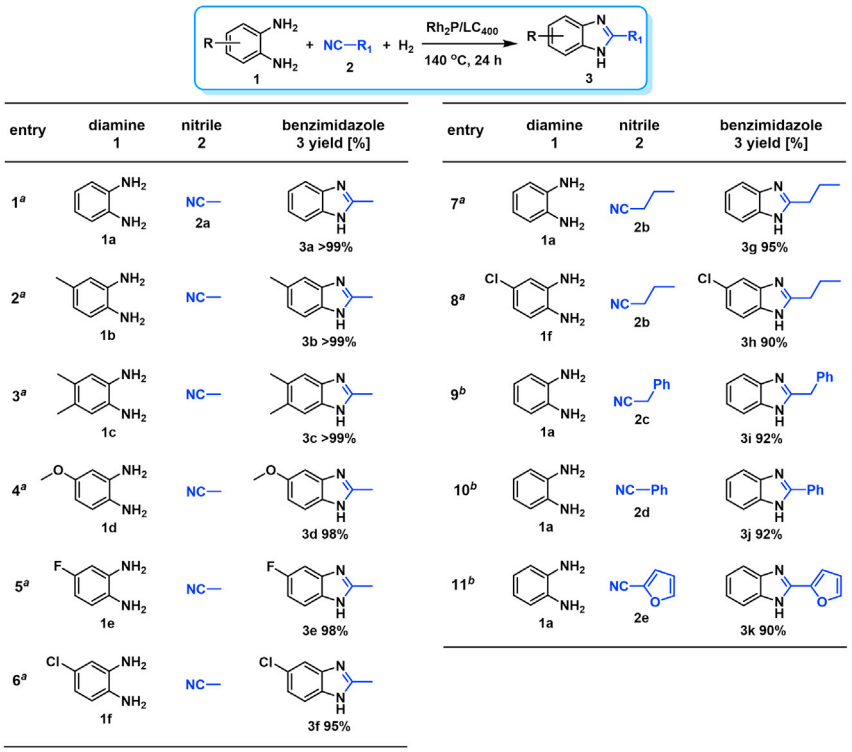

Figure 8. Scope of diamines and nitriles for hydrogenative coupling

[a]Performed with Rh_2P/LC_{400} (20 mg), **1** (0.3 mmol), **2** (3.0 mL), P_{H2} (1.0 MPa). [b]**2** (3.0 mmol) in THF (3.0 mL) was used instead of **2** (3.0 mL).

corresponding benzimidazoles (**3a**–**f**) in excellent yields. The substituted **1a** bearing electron-donating groups (CH_3, OCH_3; **1b**–**d**) and electron-withdrawing groups (F, Cl; **1e**–**f**) were all selectively and quantitatively transformed into the corresponding **3** with the current catalytic system. Notably, in the case of 4-chloro-1,2-phenylenediamine (**1f**), dehalogenation products were unobserved. In addition to CH_3CN, various nitriles such as *n*-butylnitrile (**2b**), phenylacetonitrile (**2c**), benzonitrile (**2d**), and 2-furonitrile (**2e**) were also applicable to the hydrogenative coupling system by affording excellent yields of the corresponding 2-alkylbenzimidazoles (**3g**–**k**). THF solvent was used when the reductive couplings were performed with **2c**–**e**. The above results thus demonstrated that the developed Rh_2P/LC_{400} catalyst enables highly selective and efficient synthesis of various 2-alkylbenzimidazoles by the hydrogenative coupling of the corresponding nitriles and aromatic 1,2-diamines (Figures S10–S20). In addition to 2-alkylbenzimidazoles, 2-unsubstituted benzimidazoles were recently reported in 35–86% yields with a wide tolerance of functional groups by a direct coupling of **1** with dimethyl sulfoxide (DMSO), in which DMSO functions as methyne source, oxidant, and solvent (Zhu et al., 2020). These two synthetic methods thus highlight a powerful and important extension to benzimidazoles in a sustainable and green way.

Proposed reaction mechanism

Finally, Scheme 2B shows proposed hydrogenative coupling mechanism with Rh_2P/LC_{400} catalyst for **3** formation. Hydrogenation (with H_2) and transfer hydrogenation (with N_2H_4) of nitrile **2** lead to formation imine intermediate **6** and primary amine **7**. Subsequent reaction of **1** with **6** results in **11** with elimination of NH_3. Cyclization of **11** followed by catalytic dehydrogenation of intermediate **12** give **3** with aromatization as a driven force. Moreover, **7** reacts with **6** leading to the formation of secondary imine **8** with exclusion of NH_3. A successive reaction of **8** with **1** also yields **11** with release of **7**. Notably, an equivalent amount of H_2 to nitrile molecule is required to initialize the reaction. However, an equivalent H_2 is finally released from dehydrogenative aromatization step for **3** formation. Therefore, "hydrogen-borrowing" (HB) mechanism is involved in the coupling reaction. The reductive coupling reaction is thus initialized from nitrile-activation by hydrogenation.

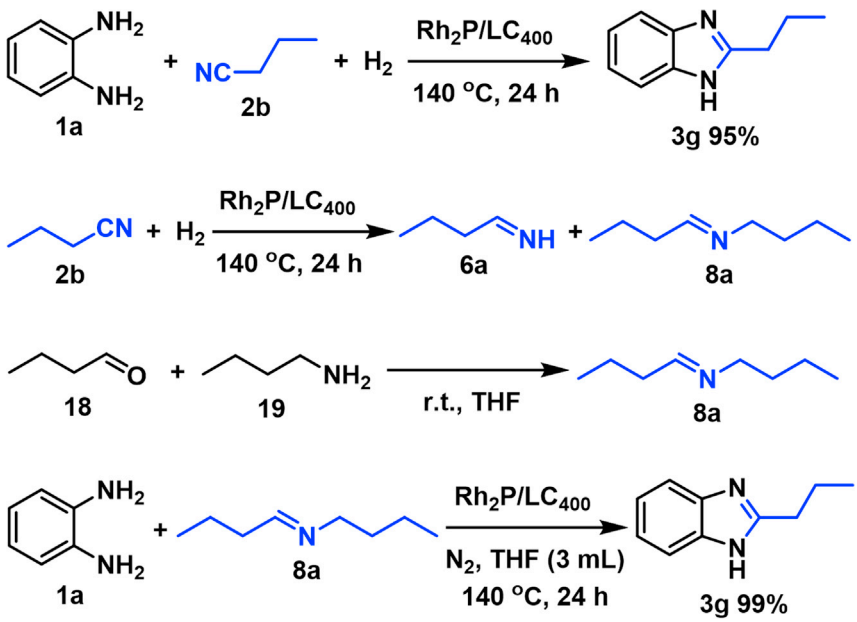

Scheme 5. Controlled experiments for mechanism investigation

Controlled experiments were then performed for mechanism investigation (Scheme 5). Our coupling scope experiments have demonstrated that hydrogenative coupling of **2b** with **1a** led to 2-propyl-1*H*-benzo[*d*] imidazole (**3g**) formation in excellent yield. According to above proposed mechanism (Scheme 2B), the reductive coupling process should be initialized from catalytic hydrogenation of **2b** with butan-1-imine (**6a**) and *N*-butylbutan-1-imine (**8a**) as the intermediates (Scheme 5). Due to high reactivity of **6a**, **8a** (Figure S9) was instead directly prepared by condensation of *n*-butyl aldehyde (**18**) and *n*-butylamine (**19**). As expected, treatment **8a** with **1a** in the presence of Rh_2P/LC_{400} quantitatively afforded **3g** under N_2 atmosphere in THF, thus demonstrating intermediate nature of **8a**. Rh_2P/LC_{400} mainly promoted catalytic dehydrogenation process for aromatization under such conditions. Our controlled experiments thus suggested the mechanism as shown in Scheme 2B.

In summary, a direct reductive coupling of nitriles and 1,2-phenylenediamines was readily achieved with Rh_2P catalyst to give various benzimidazoles in excellent yields (95%–99%). Both H_2 and $N_2H_4 \cdot H_2O$ are effective hydrogen sources for the reductive coupling reaction. The high efficiency of Rh_2P in the reaction is presumably attributed to the enhanced charge transfer to Rh, as well as strong interactions between P and Rh. Isotope trace experiments confirmed the presence of H/D exchange in reductive coupling between H_2 and the inert $-CD_3$ group of CD_3CN *via* an intramolecular D-shift. The Rh_2P catalyst can be easily recycled at least for seven times without any significant deactivations. This efficient and convenient method should have great impact on the synthesis of benzimidazole-based heterocyclic compounds.

Limitations of the study

The developed reductive coupling reaction works well with various 1,2-diamines and nitriles to give the corresponding benzimidazoles. However, the hydrogenative coupling of 3,4-diaminobenzonitrile with CH_3CN led to formation a serial of products with full conversion of 3,4-diaminobenzonitrile, suggesting a complicated competition between hydrogenation, hydrogenolysis, ethylation and consecutive ethylation. Direct co-coupling of 3,4-diaminobenzonitrile was unobserved in THF solvent in the absence of CH_3CN. The detailed reason is still not clear.

STAR★METHODS

Detailed methods are provided in the online version of this paper and include the following:

- KEY RESOURCES TABLE
- RESOURCE AVAILABILITY

- Lead contact
- Materials availability
- Data and code availability
- METHOD DETAILS
  - Materials synthesis
  - General procedure
  - Characterization of products 3a-3k (NMR data)

SUPPLEMENTAL INFORMATION

Supplemental information can be found online at https://doi.org/10.1016/j.isci.2021.103045.

ACKNOWLEDGMENTS

This research is financially supported by National Natural Science Foundation of China (Grant No. 22075104, U1810111, 21676089), Science and Technology Planning Project of Guangdong Province-China (2015A010106010), and Youth Science and Technology Innovation Talent of Guangdong TeZhi Plan (Grant No. 2019TQ05L111).

AUTHOR CONTRIBUTIONS

J.C. designed and directed the investigations. J.C., T.L., and Y.X. composed the manuscript. J.Z. developed the catalytic method. R.Y. studied the substrate scope. All the authors were involved the analysis of results and discussions of the project.

DECLARATION OF INTERESTS

The authors declare no competing interests.

Received: May 15, 2021
Revised: July 21, 2021
Accepted: August 24, 2021
Published: September 24, 2021

REFERENCES

Alvarado Rupflin, L., Mormul, J., Lejkowski, M., Titlbach, S., Papp, R., Gläser, R., Dimitrakopoulou, M., Huang, X., Trunschke, A., Willinger, M.G., et al. (2017). Platinum group metal phosphides as heterogeneous catalysts for the gas-phase hydroformylation of small olefins. ACS Catal. *7*, 3584–3590.

An, W.-K., Zheng, S.-J., Zhang, H.-X., Shang, T.-T., Wang, H.-R., Xu, X.-J., Jin, Q., Qin, Y., Ren, Y., Jiang, S., et al. (2021). s-Tetrazine-functionalized hyper-crosslinked polymers for efficient photocatalytic synthesis of benzimidazoles. Green. Chem. *23*, 1292–1299.

Anet, F.A.L., and O'Leary, D.J. (1989). H-D coupling constants and deuterium isotope effects on the proton chemical shifts in partially deuteriated methanes. Tetrahedron Lett. *30*, 2755–2758.

Bagal, D.B., and Bhanage, B.M. (2015). Recent advances in transition metal-catalyzed hydrogenation of nitriles. Adv. Synth. Catal. *357*, 883–900.

Braos-García, P., García-Sancho, C., Infantes-Molina, A., Rodríguez-Castellón, E., and Jiménez-López, A. (2010). Bimetallic Ru/Ni supported catalysts for the gas phase hydrogenation of acetonitrile. Appl. Catal. A-gen. *381*, 132–144.

Carothers, W.H., and Jones, G.A. (1925). The preparation of some primary amines by the catalytic reduction of nitriles. J. Am. Chem. Soc. *47*, 3051–3057.

Chakrabarti, K., Maji, M., and Kundu, S. (2019). Cooperative iridium complex catalyzed synthesis of quinoxalines, benzimidazoles and quinazolines in water. Green. Chem. *21*, 1999–2004.

Chakraborty, S., and Berke, H. (2014). Homogeneous hydrogenation of nitriles catalyzed by molybdenum and tungsten amides. ACS Catal. *4*, 2191–2194.

Chakraborty, S., and Milstein, D. (2017). Selective hydrogenation of nitriles to secondary imines catalyzed by an iron pincer complex. ACS Catal. *7*, 3968–3972.

Chatterjee, S., and Saito, T. (2015). Lignin-derived advanced carbon materials. ChemSusChem *8*, 3941–3958.

Chen, M., Wu, Q., Lin, C., Zhang, J., Zhao, J., Chen, J., and Xu, Y. (2020). Chemical fixation of CO_2 using highly dispersed Cu on hierarchically porous N-doped carbon. ACS Appl. Mater. Inter. *12*, 40236–40247.

Chen, Y.-Y., Zhang, Y., Jiang, W.-J., Zhang, X., Dai, Z., Wan, L.-J., and Hu, J.-S. (2016). Pomegranate-like N,P-doped Mo_2C@C nanospheres as highly active electrocatalysts for alkaline hydrogen evolution. ACS Nano *10*, 8851–8860.

Dalziel, M.E., Deichert, J.A., Carrera, D.E., Beaudry, D., Han, C., Zhang, H., and Angelaud, R. (2018). Magnesium ethoxide promoted conversion of nitriles to amidines and its application in 5,6-dihydroimidazobenzoxazepine synthesis. Org. Lett. *20*, 2624–2627.

Deng, J., Xiong, T., Xu, F., Li, M., Han, C., Gong, Y., Wang, H., and Wang, Y. (2015). Inspired by bread leavening: one-pot synthesis of hierarchically porous carbon for supercapacitors. Green. Chem. *17*, 4053–4060.

Denny, B.J., Wheelhouse, R.T., Stevens, M.F.G., Tsang, L.L.H., and Slack, J.A. (1994). NMR and molecular modeling investigation of the mechanism of activation of the antitumor drug temozolomide and its interaction with DNA. Biochemistry *33*, 9045–9051.

Duan, H., Li, D., Tang, Y., He, Y., Ji, S., Wang, R., Lv, H., Lopes, P.P., Paulikas, A.P., Li, H., et al. (2017). High-performance Rh_2P electrocatalyst for efficient water splitting. J. Am. Chem. Soc. *139*, 5494–5502.

Feng, F., Ye, J., Cheng, Z., Xu, X., Zhang, Q., Ma, L., Lu, C., and Li, X. (2016). Cu-Pd/γ-Al_2O_3 catalyzed the coupling of multi-step reactions:

direct synthesis of benzimidazole derivatives. RSC Adv. *6*, 72750–72755.

Gan, Z., Tian, Q., Shang, S., Luo, W., Dai, Z., Wang, H., Li, D., Wang, X., and Yuan, J. (2018). Imidazolium chloride-catalyzed synthesis of benzimidazoles and 2-substituted benzimidazoles from *o*-phenylenediamines and DMF derivatives. Tetrahedron *74*, 7450–7456.

Griffin, M.B., Baddour, F.G., Habas, S.E., Nash, C.P., Ruddy, D.A., and Schaidle, J.A. (2017). An investigation into support cooperativity for the deoxygenation of guaiacol over nanoparticle Ni and Rh_2P. Catal. Sci. Technol. *7*, 2954–2966.

Hayes, J.R., Bowker, R.H., Gaudette, A.F., Smith, M.C., Moak, C.E., Nam, C.Y., Pratum, T.K., and Bussell, M.E. (2010). Hydrodesulfurization properties of rhodium phosphide: comparison with rhodium metal and sulfide catalysts. J. Catal. *276*, 249–258.

Hirota, K., and Hironaka, Y. (1965). The chemisorbed state of propene on metals in reference to the catalytic hydrogenation. J. Catal. *4*, 602–607.

Hölljes, E.L., and Wagner, E.C. (1944). Some reactions of nitriles as acid anammonides[1]. J. Org. Chem. *9*, 31–49.

Horn, R.R., and Everett, G.W. (1971). Proton and deuteron nuclear magnetic resonance isotope shifts in partially deuterated tris(2,4-pentanedionato)vanadium(III). J. Am. Chem. Soc. *93*, 7173–7178.

Hou, S.-F., Chen, J.-Y., Xue, M., Jia, M., Zhai, X., Liao, R.-Z., Tung, C.-H., and Wang, W. (2020). Cooperative molybdenum-thiolate reactivity for transfer hydrogenation of nitriles. ACS Catal. *10*, 380–390.

Huang, Y., and Sachtler, W.M.H. (1999a). Concerted reaction mechanism in deuteration and H/D exchange of nitriles over transition metals. J. Catal. *184*, 247–261.

Huang, Y., and Sachtler, W.M.H. (1999b). On the mechanism of catalytic hydrogenation of nitriles to amines over supported metal catalysts. Appl. Catal. A Gen. *182*, 365–378.

Islam, M., Mondal, P., Singha Roy, A., and Tuhina, K. (2010). Catalytic hydrogenation of various organic substrates using a reusable plymer-anchored palladium(II) complex. J. Mater. Sci. *45*, 2484–2493.

Keri, R.S., Hiremathad, A., Budagumpi, S., and Nagaraja, B.M. (2015). Comprehensive review in current developments of benzimidazole-based medicinal chemistry. Chem. Biol. Drug Des. *86*, 19–65.

Komanoya, T., Kinemura, T., Kita, Y., Kamata, K., and Hara, M. (2017). Electronic effect of ruthenium nanoparticles on efficient reductive amination of carbonyl compounds. J. Am. Chem. Soc. *139*, 11493–11499.

Kundu, M.K., Mishra, R., Bhowmik, T., and Barman, S. (2018). Rhodium metal–rhodium oxide ($Rh–Rh_2O_3$) nanostructures with Pt-like or better activity towards hydrogen evolution and oxidation reactions (HER, HOR) in acid and base: correlating its HOR/HER activity with hydrogen binding energy and oxophilicity of the catalyst. J. Mater. Chem. A. *6*, 23531–23541.

Kunin, A.J., Nanni, E.J., and Eisenberg, R. (1985). Chemical reduction of bis [bis(diphenylphosphino)ethane]rhodium(1+), $[Rh(dppe)_2]^+$. characterization of $Rh(dppe)_2^0$ and $Rh(dppe)_2^-$. Inorg. Chem. *24*, 1852–1856.

Le Questel, J.-Y., Berthelot, M., and Laurence, C. (2000). Hydrogen-bond acceptor properties of nitriles: a combined crystallographic and *ab initio* theoretical investigation. J. Phys. Org. Chem. *13*, 347–358.

Li, C., Yang, M., Liu, Z., Zhang, Z., Zhu, T., Chen, X., Dong, Y., and Cheng, H. (2020a). $Ru-Ni/Al_2O_3$ bimetallic catalysts with high catalytic activity for *N*-propylcarbazole hydrogenation. Catal. Sci. Technol. *10*, 2268–2276.

Li, J., Tian, Q., Jiang, S., Zhang, Y., and Wu, Y. (2016). Electrocatalytic performances of phosphorus doped carbon supported Pd towards formic acid oxidation. Electrochim. Acta *213*, 21–30.

Li, Y., Gong, Y., Xu, X., Zhang, P., Li, H., and Wang, Y. (2012). A practical and benign synthesis of amines through $Pd@mpg-C_3N_4$ catalyzed reduction of nitriles. Catal. Commun. *28*, 9–12.

Li, Z., Ye, Z., Chen, L., Cui, J., and Chen, J. (2020b). Hierarchically nanoporous titanium-based coordination polymers for photocatalytic synthesis of benzimidazole. ACS Appl. Nano Mater. *3*, 10720–10731.

Lin, C., Wan, W., Wei, X., and Chen, J. (2021). H_2 activation with Co nanoparticles encapsulated in N-doped carbon nanotubes for green synthesis of benzimidazoles. ChemSusChem *14*, 709–720.

Liu, L., Liu, Y., Ai, Y., Li, J., Zhou, J., Fan, Z., Bao, H., Jiang, R., Hu, Z., Wang, J., et al. (2018a). Pd-CuFe catalyst for transfer hydrogenation of nitriles: controllable selectivity to primary amines and secondary amines. iScience *8*, 61–73.

Liu, W., Sahoo, B., Junge, K., and Beller, M. (2018b). Cobalt complexes as an emerging class of catalysts for homogeneous hydrogenations. Acc. Chem. Res. *51*, 1858–1869.

Luo, F., Guo, L., Xie, Y., Xu, J., Cai, W., Qu, K., and Yang, Z. (2020). Robust hydrogen evolution reaction activity catalyzed by ultrasmall Rh-Rh2P nanoparticles. J. Mater. Chem. A. *8*, 12378–12384.

Monguchi, Y., Mizuno, M., Ichikawa, T., Fujita, Y., Murakami, E., Hattori, T., Maegawa, T., Sawama, Y., and Sajiki, H. (2017). Catalyst-dependent selective hydrogenation of nitriles: selective synthesis of tertiary and secondary amines. J. Org. Chem. *82*, 10939–10944.

Naito, S., and Tanimoto, M. (1999). Mechanistic study of the hydrogen exchange and hydrogenation of propene over alumina supported rhodium and ruthenium carbonyl cluster complexes. J. Mol. Catal. A Chem. *141*, 205–214.

Nakajima, K., Noma, R., Kitano, M., and Hara, M. (2013). Titania as an early transition metal oxide with a high density of Lewis acid sites workable in water. J. Phys. Chem. C *117*, 16028–16033.

Nandi, S., Patel, P., Jakhar, A., Khan, N.H., Biradar, A.V., Kureshy, R.I., and Bajaj, H.C. (2017). Cucurbit[6]uril-stabilized palladium nanoparticles as a highly active catalyst for chemoselective hydrogenation of various reducible groups in aqueous media. ChemistrySelect *2*, 9911–9919.

Osborn, J.A., and Wilkinson, G. (1967). Tris(triphenylphosphine)halorhodium(I). Inorg. Synth. *10*, 67–71.

Selvam, K., Krishnakumar, B., Velmurugan, R., and Swaminathan, M. (2009). A simple one pot nano titania mediated green synthesis of 2-alkylbenzimidazoles and indazole from aromatic azides under UV and solar light. Catal. Commun. *11*, 280–284.

Shi, Y., and Zhang, B. (2016). Recent advances in transition metal phosphide nanomaterials: synthesis and applications in hydrogen evolution reaction. Chem. Soc. Rev. *45*, 1529–1541.

Shiraishi, Y., Sugano, Y., Tanaka, S., and Hirai, T. (2010). One-pot synthesis of benzimidazoles by simultaneous photocatalytic and catalytic reactions on $Pt@TiO_2$ nanoparticles. Angew. Chem. *122*, 1700–1704.

Sriramoju, V., Kurva, S., and Madabhushi, S. (2018). Oxone-mediated annulation of 2-aminobenzamides and 1,2-diaminobenzenes with *sec*-amines *via* imine-*N*-oxides: new syntheses of 2,3-dihydroquinazolin-4(1*H*)-ones and 1*H*-benzimidazoles. New J. Chem. *42*, 3188–3191.

Su, J., Zhao, H., Fu, W., Tian, W., Yang, X., Zhang, H., Ling, F., and Wang, Y. (2020). Fine rhodium phosphides nanoparticles embedded in N, P dual-doped carbon film: new efficient electrocatalysts for ambient nitrogen fixation. Appl. Catal. B Environ. *265*, 118589–118596.

Sun, W., Wu, S., Lu, Y., Wang, Y., Cao, Q., and Fang, W. (2020). Effective control of particle size and electron density of Pd/C and Sn-Pd/C nanocatalysts for vanillin production via base-free oxidation. ACS Catal. *10*, 7699–7709.

Tamura, M., Honda, M., Noro, K., Nakagawa, Y., and Tomishige, K. (2013). Heterogeneous CeO_2-catalyzed selective synthesis of cyclic carbamates from CO_2 and aminoalcohols in acetonitrile solvent. J. Catal. *305*, 191–203.

Wade, A.R., Pawar, H.R., Biware, M.V., and Chikate, R.C. (2015). Synergism in semiconducting nanocomposites: visible light photocatalysis towards the formation of C–S and C–N bonds. Green. Chem. *17*, 3879–3888.

Wan, Y., Zhang, Z., Ma, N., Bi, J., and Zhang, G. (2019). Acylamino-directed specific sequential difunctionalizations of anilides via metal-free relay reactions for *p*-oxygen and *o*-nitrogen incorporation. J. Org. Chem. *84*, 780–791.

Wang, H., Partch, R.E., and Li, Y. (1997). Synthesis of 2-alkylbenzimidazoles via TiO_2-mediated photocatalysis. J. Org. Chem. *62*, 5222–5225.

Wang, K., Jiang, P., Yang, M., Ma, P., Qin, J., Huang, X., Ma, L., and Li, R. (2019). The metal-free nitrogen-doped carbon nanosheets: a catalyst for directly synthesis imines under mild conditions. Green. Chem. *21*, 2448–2461.

Wang, Y., Zhu, Q., Xie, T., Peng, Y., Liu, S., and Wang, J. (2020). Promoted alkaline hydrogen evolution reaction performance of Ru/C by introducing TiO2 nanoparticle. ChemElectroChem *7*, 1182–1186.

Werkmeister, S., Junge, K., and Beller, M. (2014). Catalytic hydrogenation of carboxylic acid esters, amides, and nitriles with homogeneous catalysts. Org. Process. Res. Dev. *18*, 289–302.

Wheelhouse, R.T., and Stevens, M.F.G. (1993). Decomposition of the antitumour drug temozolomide in deuteriated phosphate buffer: methyl group transfer is accompanied by deuterium exchange. J. Chem. Soc. Chem. Commun. 1177–1178.

Yamini, Sharma, S., and Das, P. (2021). Rhodium catalyzed 2-alkyl-benzimidazoles synthesis from benzene-1,2-diamines and tertiary alkylamines as alkylating agents. Appl. Organomet. Chem. *35*, e6278.

Yates, J.T., Duncan, T.M., Worley, S.D., and Vaughan, R.W. (1979). Infrared spectra of chemisorbed CO on Rh. J. Chem. Phys. *70*, 1219–1224.

Zhang, Y., Yang, H., Chi, Q., and Zhang, Z. (2019). Nitrogen-doped carbon supported nickel nanoparticles: a robust catalyst to bridge the hydrogenation of nitriles and the reductive amination of carbonyl compounds. ChemSusChem *12*, 1246–1255.

Zhao, J.P., Hernández, W.Y., Zhou, W.J., Yang, Y., Vovk, E.I., Wu, M., Naghavi, N., Capron, M., and Ordomsky, V. (2020). Nanocell type Ru@quinone core-shell catalyst for selective oxidation of alcohols to carbonyl compounds. Appl. Catal. A-gen. *602*, 117693–117700.

Zhu, X., Zhang, F., Kuang, D., Deng, G., Yang, Y., Yu, J., and Liang, Y. (2020). K_2S as sulfur source and DMSO as carbon source for the synthesis of 2-unsubstituted benzothiazoles. Org. Lett. *22*, 3789–3793.

Zhu, Y., Li, Z., and Chen, J. (2019). Applications of lignin-derived catalysts for green synthesis. Green. Energy Environ *4*, 210–244.

Zhuang, M., Ou, X., Dou, Y., Zhang, L., Zhang, Q., Wu, R., Ding, Y., Shao, M., and Luo, Z. (2016). Polymer-embedded fabrication of Co_2P nanoparticles encapsulated in N,P-doped graphene for hydrogen generation. Nano Lett. *16*, 4691–4698.

Zou, J., Wu, M., Ning, S., Huang, L., Kang, X., and Chen, S. (2019). Ru@Pt core-shell nanoparticles: impact of the atomic ordering of Ru metal core on the electrocatalytic activity of Pt shell. ACS Sustain. Chem. Eng. *7*, 9007–9016.

STAR★METHODS

KEY RESOURCES TABLE

REAGENT or RESOURCE	SOURCE	IDENTIFIER
Chemicals, peptides, and recombinant proteins		
$RhCl_3 \cdot xH_2O$	Aladdin Co. Ltd.	CAS 20765-98-4
$PdCl_2$	Aladdin Co. Ltd.	CAS 7647-10-1
$RuCl_3 \cdot xH_2O$	Aladdin Co. Ltd.	CAS 14898-67-0
$N_2H_4 \cdot H_2O$	Aladdin Co. Ltd.	CAS 7803-57-8
Aniline	Aladdin Co. Ltd.	CAS 62-53-3
Butyronitrile	Aladdin Co. Ltd.	CAS 109-74-0
Phenylacetonitrile	Aladdin Co. Ltd.	CAS 140-29-4
Benzonitrile	Aladdin Co. Ltd.	CAS 100-47-0
2-Furonitrile	Aladdin Co. Ltd.	CAS 617-90-3
Benzylamine	Aladdin Co. Ltd.	CAS 100-46-9
Ethylenediamine	Aladdin Co. Ltd.	CAS 107-15-3
1,2-Diaminocyclohexane	Aladdin Co. Ltd.	CAS 694-83-7
1,4-Diaminobutane	Aladdin Co. Ltd.	CAS 110-60-1
Butylamine	Aladdin Co. Ltd.	CAS 109-73-9
Butyraldehyde	Aladdin Co. Ltd.	CAS 123-72-8
Acetonitrile	Guangzhou Kutai Trade Co. Ltd	CAS 75-05-8
Tetrahydrofuran	Guangzhou Kutai Trade Co. Ltd	CAS 109-99-9
High purity gases H_2($\geq$99.9%)	Guangzhou Yinglai Gas Co. Ltd.	CAS 1333-74-0
High purity gases N_2($\geq$99.9%)	Guangzhou Yinglai Gas Co. Ltd.	CAS 7727-37-9
1,2-Phenylenediamine	Macklin Biochemical Science Co. Ltd.	CAS 95-54-5
3,4-Diaminotoluene	Bide Pharmatech Co. Ltd.	CAS 496-72-0
4,5-Dimethylbenzene-1,2-diamine	Bide Pharmatech Co. Ltd.	CAS 3171-45-7
4-Methoxy-o-phenylenediamine	Bide Pharmatech Co. Ltd.	CAS 102-51-2
4-Fluorobenzene-1,2-diamine	Bide Pharmatech Co. Ltd.	CAS 367-31-7
4-Chlorobenzene-1,2-diamine	Bide Pharmatech Co. Ltd.	CAS 95-83-0
Other		
Optima 2000 DV inductively coupled plasma atomic emission spectrometer (ICP-AES)	PerkinElmer, USA	https://www.perkinelmer.com.cn
Vertex 70 FI-TR spectrometer	Bruker	https://bruker.com
ULTRA 55 Scanning Electron Microscope (SEM)	Zeiss	http://www.lingm.com
TECNAL-12 Transmission Electron Microscope (TEM)	FEI	https://www.thermofisher.cn
TriStar II 3flex adsorption analyzer	Micromeritics	https://www.micromeritics.com
D8 ADVANCE X-ray Powder Diffractometer (XRD)	Bruker	https://bruker.com
K-Alpha X-Ray photoelectron spectrometer (XPS)	Thermo scientific	https://www.thermofisher.cn
Fuli 9790 (Type II) Gas Chromatography (GC)	Fuli Instruments	http://www.cnfuli.com.cn
GC-2010 Plus Gas Chromatography-Mass Spectrometer (GC-MS)	Shimadzu Corporation of Japan	https://www.shimadzu.com/
AV III 300 (300 MHz) spectrometer	Bruker	https://bruker.com

RESOURCE AVAILABILITY

Lead contact

Further information and requests for resources and reagents should be directed to and will be fulfilled by the lead contact, Jinzhu Chen (chenjz@jnu.edu.cn).

Materials availability

This work did not generate new unique reagents. All stable reagents generated in this study are available from the lead contact without restriction.

Data and code availability

Original code was not used in this manuscript. All relevant data supporting the findings of this study are available within the paper and its Supplemental Information files. Any additional information required to reanalyze the data reported in this paper is available from the lead contact upon reasonable request.

METHOD DETAILS

Materials synthesis

Preparation of $Rh(PPh_3)_3Cl$ and $Rh(dppe)_2Cl$: $Rh(PPh_3)_3Cl$ and $Rh(dppe)_2Cl$ were prepared according to literature methods (Osborn and Wilkinson, 1967; Kunin et al., 1985).

Preparation of LC: LC was prepared according to the literature method with slight modification (Chen et al., 2020), enzymatic hydrolysis lignin (EHL, 3.0 g) and potassium bicarbonate (6.0 g) were finely grinded and mixed uniformly in a mortar. The resulting mixture was then transferred into an alundum boat and calcined under nitrogen atmosphere at 800°C for 3 h with a heating rate of 2°C min^{-1}. The obtained black solid was collected, grinded into black powder, and further leached with aqueous HCl solution (100 mL, 2 mol L^{-1}) for 12 h with vigorous stirring at room temperature. LC was then obtained as black solid (about 300 mg) by solution filtration, thoroughly washed with water (1 L), and dried at 80°C under the vacuum overnight.

Preparation of Rh_2P/LC_{400}: $RhCl_3 \cdot xH_2O$ (25 mg, 0.095 mmol) and 1,2-*bis*(diphenylphosphino)ethane (dppe, 150 mg, 0.38 mmol) were dissolved in tetrahydrofuran (THF, 80 mL) in a round bottom flask. LC (150 mg) was subsequently added into the above solution, the resulting mixture was vigorously stirred at 60°C for 12 h. THF solvent in the mixture was then removed by rotary evaporator under reduced pressure. The obtained mixture was transferred into a quartz boat and calcined under atmospheric mixture of H_2/N_2 (V_{H2}:V_{N2} = 8%) for 2 h at 400°C with a heating rate of 5°C min^{-1} to give Rh_2P/LC_{400} (Rh, 4.8 wt.%). The Rh content was obtained by inductively coupled plasma-atomic emission spectrometry (ICP-AES) analysis.

Preparation of Rh/LC_{400}: Rh/LC_{400} (Rh, 5.5 wt.%) was prepared with the same procedure used for Rh_2P/LC_{400} without addition of dppe.

Preparation of Pd/LC_{400}: Pd/LC_{400} (Pd, 5.2 wt.%) was prepared with the same procedure used for Rh_2P/LC_{400} except that $RhCl_3 \cdot xH_2O$ (25 mg) and THF solvent were respectively replaced by $PdCl_2$ (25 mg) and acetonitrile solvent.

Preparation of Ru/LC_{400}: Ru/LC_{400} (Ru, 5.1 wt.%) was prepared with the same procedure used for Rh_2P/LC_{400} except that $RhCl_3 \cdot xH_2O$ (25 mg) was replaced by $RuCl_3 \cdot xH_2O$ (25 mg).

General procedure

Reductive coupling: Typically, Rh_2P/LC_{400} (20 mg), 1,2-phenylenediamine (**1a**, 32 mg, 0.3 mmol) and acetonitrile (**2a**, 3.0 mL) were added into a Teflon-lined autoclave reactor (25 mL). Then, H_2 (0.5 MPa) was slowly loaded into the reactor to remove the air inside for three times. Finally, H_2 (1.0 MPa) was slowly charged into the reactor at ambient temperature. The reductive coupling was performed for 24 h at 140°C. After the reaction, the obtained mixture was analyzed by Gas Chromatography.

*Calculation of **1a** conversion and **3a** yield:* After the reaction, the mixture was filtered to remove catalyst, the resulting filtrate was then transferred into a volumetric flask, diluted to the volume with acetonitrile, and finally analyzed by GC. **1a** conversion and **3a** yield were then obtained by the corresponding formulas:

$$1a\ conversion(\%) = \left(\frac{moles\ of\ 1a\ converted}{moles\ of\ 1a\ fed}\right) \times 100$$

$$3a\ yield(\%) = \left(\frac{moles\ of\ 3a\ produced}{moles\ of\ 1a\ fed}\right) \times 100$$

Characterization of products 3a-3k (NMR data)

2-Methyl-1H-benzo[*d*]imidazole 3a.

3a

Yield: 39.3 mg (99%). ^{1}H NMR (300 MHz, CD_3CN, 25°C) δ 7.48 (dd, *J* = 6.0, 3.2 Hz, 2H), 7.15 (dd, *J* = 6.0, 3.2 Hz, 2H), 2.52 (s, 3H). ^{13}C {^{1}H} NMR (75 MHz, $CDCl_3$, 25°C) δ = 151.28, 138.77, 122.32, 114.63, 15.13 ppm. The spectral data is consistent with the literature data (, 2020b).

2,5-Dimethyl-1H-benzo[*d*]imidazole. 3b.

3b

Yield: 43.5 mg (99%). ^{1}H NMR (300 MHz, DMSO-d_6, 25°C) δ 7.35 (d, *J* = 8.1 Hz, 1H), 7.25 (s, 1H), 6.95 (d, *J* = 8.1 Hz, 1H), 2.47 (s, 3H), 2.38 (s, 3H). ^{13}C {^{1}H} NMR (75 MHz, DMSO, 25°C) δ 150.81, 138.19, 136.79, 130.35, 122.65, 114.01, 113.63, 21.30, 14.40. The spectral data is consistent with the literature data (Gan et al., 2018).

2,5,6-Trimethyl-1H-benzo[*d*]imidazole. 3c.

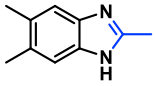

3c

Yield: 47.6 mg (99%). ^{1}H NMR (300 MHz, DMSO-d_6, 25°C) δ 7.20 (s, 2H), 2.43 (s, 3H), 2.27 (s, 6H). ^{13}C {^{1}H} NMR (75 MHz, DMSO-d_6, 25°C) δ 150.16, 129.06, 19.88, 14.57. The spectral data is consistent with the literature data (Gan et al., 2018).

5-Methoxy-2-methyl-1H-benzo[*d*]imidazole. 3d.

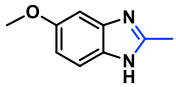

3d

Yield: 47.7 mg (98%). ^{1}H NMR (300 MHz, DMSO-d_6, 25°C) δ 7.33 (d, *J* = 8.6 Hz, 1H), 6.96 (s, 1H), 6.74 (d, *J* = 10.7 Hz, 1H), 3.75 (s, 3H), 2.44 (s, 3H). ^{13}C {^{1}H} NMR (75 MHz, DMSO-d_6, 25°C) δ 155.08, 150.80, 110.08, 55.41, 14.64. The spectral data is consistent with the literature data (Wan et al., 2019).

5-Fluoro-2-methyl-1H-benzo[*d*]imidazole. 3e.

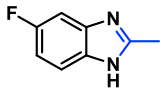

3e

Yield: 44.1 mg (98%). ^{1}H NMR (300 MHz, DMSO-d_6, 25°C) δ 7.45 (dd, *J* = 8.6, 4.9 Hz, 1H), 7.27 (d, *J* = 9.6 Hz, 1H), 6.98 (t, *J* = 9.3 Hz, 1H), 2.47 (s, 3H). ^{13}C {^{1}H} NMR (75 MHz, DMSO-d_6, 25°C) δ 159.69, 156.59, 152.81, 109.00, 108.67, 40.80, 14.65. The spectral data is consistent with the literature data (Yamini et al., 2021).

5-Chloro-2-methyl-1H-benzo[*d*]imidazole. **3f**.

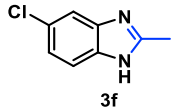

3f

Yield: 47.5 mg (95%). ^{1}H NMR (300 MHz, DMSO-d_6, 25°C) δ 7.50 (s, 1H), 7.45 (d, J = 8.5 Hz, 1H), 7.14 (d, J = 8.5 Hz, 1H), 2.48 (s, 3H). ^{13}C {^{1}H} NMR (75 MHz, DMSO-d_6, 25°C) δ 153.00, 125.48, 121.25, 115.13, 114.22, 14.63. The spectral data is consistent with the literature data (Gan et al., 2018).

2-Propyl-1H-benzo[*d*]imidazole. **3g**.

3g

Yield: 45.6 mg (95%). ^{1}H NMR (300 MHz, DMSO-d_6, 25°C) δ 12.18 (s, 1H), 7.45 (s, 2H), 7.09 (d, J = 5.9 Hz, 2H), 2.78 (t, J = 7.4 Hz, 2H), 1.75 (dd, J = 14.8, 7.4 Hz, 2H), 0.94 (t, J = 7.4 Hz, 3H). ^{13}C {^{1}H} NMR (75 MHz, DMSO-d_6, 25°C) δ 155.05, 121.04, 30.56, 21.03, 13.71. The spectral data is consistent with the literature data (An et al., 2021).

5-Chloro-2-propyl-1H-benzo[*d*]imidazole. **3h**.

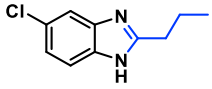

3h

Yield: 52.4 mg (90%). ^{1}H NMR (300 MHz, DMSO-d_6) δ 12.36 (s, 1H), 7.73–7.27 (m, 2H), 7.12 (s, 1H), 2.77 (t, J = 7.2 Hz, 2H), 1.77 (q, J = 7.3 Hz, 2H), 0.93 (t, J = 7.2 Hz, 3H). ^{13}C {^{1}H} NMR (75 MHz, DMSO-d_6, 25°C) δ 156.65, 125.20, 121.24, 115.26, 30.90, 20.89, 13.18. The spectral data is consistent with the literature data (Sriramoju et al., 2018).

2-Benzyl-1H-benzo[*d*]imidazole. **3i**.

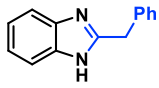

3i

Yield: 57.4 mg (92%). ^{1}H NMR (300 MHz, DMSO-d_6) δ 12.25 (s, 1H), 7.47 (dd, J = 5.8, 3.2 Hz, 2H), 7.39–7.26 (m, 4H), 7.23 (dd, J = 3.4, 2.4 Hz, 1H), 7.12 (dd, J = 5.9, 3.1 Hz, 2H), 4.17 (s, 2H). ^{13}C{^{1}H} NMR (75 MHz, DMSO-d_6) δ 153.68, 139.48, 137.10, 128.83, 126.58, 121.43, 114.71, 35.08. The spectral data is consistent with the literature data (An et al., 2021).

2-Phenyl-1H-benzo[*d*]imidazole. **3j**.

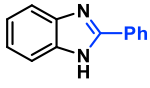

3j

Yield: 53.5 mg (92%). ^{1}H NMR (300 MHz, 25°C, DMSO-d_6) δ 12.95 (s, 1H), 8.20 (d, J = 8.2 Hz, 2H), 7.89–7.38 (m, 5H), 7.35–7.01 (m, 2H). ^{13}C{^{1}H} NMR (75 MHz, 25°C, DMSO-d_6) δ 151.25, 130.19, 129.87, 128.99, 126.46, 122.14. The spectral data is consistent with the literature data (Lin et al., 2021).

2-(2-furanyl)-1H-benzo[*d*]imidazole. **3k**.

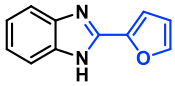

3k

Yield: 49.7 mg (90%). ^{1}H NMR (300 MHz, 25°C, DMSO-d_6) δ 12.93 (s, 1H), 7.91 (d, J = 18.7 Hz, 1H), 7.54 (s, 2H), 7.18 (d, J = 16.8 Hz, 3H), 6.69 (d, J = 19.4 Hz, 1H). ^{13}C{^{1}H} NMR (101 MHz, 25°C, DMSO-d_6) δ 145.45, 144.61, 143.55, 134.19, 122.46, 121.81, 118.72, 112.30, 111.34, 110.44. The spectral data is consistent with the literature data (Lin et al., 2021).